Fall 2020

Kinetic Monte Carlo Investigations Involving Atomic Layer Deposition of Metal-Oxide ThinFilms

David Tyler Magness
Missouri State University, tm82392@live.missouristate.edu

KINETIC MONTE CARLO INVESTIGATIONS INVOLVING ATOMIC LAYER DEPOSITION OF METAL-OXIDE THIN FILMS

A Master's Thesis

Presented to

The Graduate College of

Missouri State University

In Partial Fulfillment

Of the Requirements for the Degree

Master of Science, Materials Science

By

David Tyler Magness

December 2020

KINETIC MONTE CARLO INVESTIGATIONS INVOLVING ATOMIC LAYER DEPOSITION OF METAL-OXIDE THIN FILMS

Physics, Astronomy, and Materials Science

Missouri State University, December 2020

Master of Science

David Tyler Magness

ABSTRACT

Atomic Layer Deposition is a method of manufacturing thin film materials. Metal-oxides such as zinc-oxide and aluminum-oxide are particularly interesting candidates for use in microelectronic devices such as tunnel junction barriers, transistors, Schottky diodes, and more. By adopting a 3D Kinetic Monte Carlo model capable of simulating ZnO deposition, the effect of parameters including deposition temperature, chamber pressure, and composition of the initial substrate at the beginning of deposition can be investigated. This code generates two random numbers: One is used to select a chemical reaction to occur from a list of all possible reactions and the second is used to update the simulation clock. By using this KMC model to bridge the worlds of classical dynamics and quantum mechanics, this code can simulate physical processes that occur over time scales much longer than possible with other methods. This code has been used to demonstrate a relationship between deposition parameters and material properties including: the state of the initial surface, chamber pressure, temperature, mass gain, and atomic content which compare favorably with experimental results from the literature. The ZnO model is then combined with DFT calculations from Timo Weckman as a springboard to produce a novel KMC model capable of simulating the deposition of aluminum-oxide. These KMC investigations demonstrate the ability of this method to simulate multiple ALD techniques of interest to the materials science community.

KEYWORDS: kinetic monte carlo algorithm, atomic layer deposition, metal-oxide thin films, density functional theory, zinc-oxide, aluminum-oxide, computational materials physics

KINETIC MONTE CARLO INVESTIGATIONS INVOLVING ATOMIC LAYER DEPOSITION OF METAL-OXIDE THIN FILMS

By

David Tyler Magness

A Master's Thesis
Submitted to the Graduate College
Of Missouri State University
In Partial Fulfillment of the Requirements
For the Degree of Master of Science, Materials Science

December 2020

Approved:

Ridwan Sakidja, Ph.D., Thesis Committee Chair

Robert Mayanovic, Ph.D., Committee Member

Tiglet Besara, Ph.D., Committee Member

Julie Masterson, Ph.D., Dean of the Graduate College

ACKNOWLEDGEMENTS

My darling Ms. Korra Lynn, you are Daddy's *most favorite* subset of the Universe. Live long, prosper, and forever kick mass.

Dad, this happened because you taught me how to how to work and stay grounded whilst thinking amongst the stars. To infinity and beyond! Mom, I'm so thankful for space-time we were able to share and I wish you could read this.

Thank you to Dr. Sakidja for supervising this thesis and providing valuable experience and insight, I sincerely appreciate the opportunity to collaborate. Many thanks to Bikash Timalsina for his superb technical help. Much appreciation for the numerous mentors who helped me reach this goal, you all rock. Finally, to my students, who taught me more than I could've ever taught them.

Funding for this thesis was graciously provided by the National Science Foundation under the Electronics, Photonics, and Magnetic Devices (EPMD) Program. Computational support provided by NERSC was extremely helpful to this research.

TABLE OF CONTENTS

LIST OF TABLES

LIST OF FIGURES

1. INTRODUCTION

There is much to unpack in the title of this thesis and so a proper introduction is necessary and hopefully welcome. Atomic Layer Deposition (ALD) is a hot topic of interest in the materials science community. Kinetic Monte Carlo (KMC) simulations on the other hand are less frequent. A firm understanding of these concepts will help ease those interested in the gripping world of computational materials science get their toes wet with this method of investigation.

1.1. Motivation

In this section, the physical process of ALD is defined and its relevance to the scientific and industrial community established. The reasoning behind the use of the KMC method is also justified with a colorful tic-tac-toe analogy. This section will strive to establish the relevance of this study by pointing out applications of ALD and justify KMC as a practical avenue of investigation.

1.1.1. Applications of ALD. Atomic Layer Deposition is a form of Chemical Vapor Deposition (CVD). In CVD, vapor precursor is admitted into a chamber to interact with a substrate and deposit on its surface. The beauty of ALD is that there is typically more than one type of precursor used in an alternating sequence. These precursors are chosen so that their reactions are self-terminating. This means that the precursor does not interact with itself or with the byproducts of its reaction with the surface [1]. As a result, molecule-thin layers of materials can be deposited at a time.

The ability of ALD to produce ultra-thin layers of materials is very attractive to semi-conductor manufacturers and the technology industry. With the advent of Moore's Law, the race for smaller transistors to increase computing power has become the most evident use of this deposition technique. Field Programmable Gate Arrays (FPGAs) are made of logic gates composed of transistors. These transistors are dozens of nanometers thick.
Typical chemical vapor deposition techniques may only deposit layers hundreds of times thicker. Zinc-oxide (ZnO) and aluminum-oxide (Al_2O_3) can also be used in tunnel junction barriers, Schottky diodes, LED's, solar cells, and other ubiquitous nano-scale devices [1-3].

Another advantage of ALD is the ability to control adjustable parameters to affect the deposited material. Adjusting the temperature during or after deposition can yield samples of different properties like density, thickness, carrier concentration, and stoichiometry. These variables are typically changed to produce the type of sample desired [4-6].

1.1.2. Advantages of Computational Modeling. Computational modeling has many advantages as an investigative tool. Experimental studies suffer from a need of facilities, equipment, and materials. While a headache under pre-pandemic circumstances, at the time of writing, these obstacles give computational researchers an appreciation for this form of pandemic-proof science. With the progression of consumer-grade laptops and cloud computing, it is possible to perform computational studies from any location with minimal hardware setup. Utilizing open-source software further drives the cost per simulation to a fraction of the cost-per-deposition.

Aside from the cost and convenience benefits, computational modeling provides simulated evidence that can support our current understanding of chemical processes or shed light on gaps that may exist between theory and experiment. Comparing simulated data to

experimental results can reinforce scientific theory, reveal new chemical or physical reactions, or possibly even indicate errors in experimental results.

1.1.3. The Need for Multi-Scale Modeling. Perhaps the claim that computational modeling was an investigative tool was a lie. It is more like an investigative *toolbox*. There are a number of different methods that are used in computational materials physics. Classical molecular dynamics simulations and Density Functional Theory (DFT) calculations are two main categories of simulations in computational materials physics.

Molecular dynamics simulations rely on classical physics, in short, they repeatedly solve Newton's Laws of motion for a number of particles, typically numbering up to the hundreds. The timescale of these simulations is also logistically confined to the order of a microsecond [7]. While the number of atoms and the amount of time these molecular dynamics simulations can run is limited, countless scientific studies have focused on classical molecular dynamics to investigate chemical processes. One such as the diffusion of water on aluminum surfaces. These simulations are typically limited to timescales on the order of microseconds.

Density Functional Theory simulations are based on quantum mechanics and similarly solve Schrodinger's equation. These DFT calculations can typically include several to several dozen atoms at a time. DFT calculations are useful in a number of scientific studies, from optimization of molecular geometry to calculating optical spectra [8].

The advantage of DFT is that it provides a valuable way of performic ab initio calculations that incorporate quantum theory. As similarly mentioned with more classical methods, DFT simulations are limited to a small number of atoms and extremely short timescales typically lasting no longer than femtoseconds [9].

The need for an alternative way to simulate complex chemical reactions now becomes clear. The Kinetic Monte Carlo method is sometimes referred to as multi-scale modeling. The intent here being to combine DFT calculations with classical theory to achieve modeling on timescales ranging from the quantum scale to the engineering scale [10]. The KMC method serves as the bridge between scales.

Consider the following analogy: You are playing tic-tac-toe, depositing your O's during your turn in the same manner that a water pulse deposits water molecules onto a ZnO surface. Imagine having to relearn how to draw your O every time you took your turn. The game played this way would take forever. This is analogous to how classical simulations would play out; performing calculations at each timestep. However, this is not how a real game of tic-tac-toe is played. In reality, humans will typically learn how to draw the X's and O's before playing. By learning the action beforehand, much time is saved, and your average tic-tac-toe games don't take an eternity. This KMC method performs in the same manner. The individual chemical reactions, which occur numerous times each, are first simulated with DFT code, which can take days to finish a single calculation. The data from these DFT calculations is then fed into the input of the KMC code. The KMC code, in effect, remembers how these reactions occur, speeding up simulation time drastically.

1.2. The Physical Processes of ALD

This section outlines the physical processes of interest. There are two types of ALD studied here. The first type is the deposition of ZnO via alternating pulses of diethylzinc (DEZ) and water. The second type of ALD is the deposition of Al_2O_3 via alternating pulses of trimethyl-aluminum (TMA) and water.

In these examples the TMA and the DEZ are called metal precursors as they are the source of aluminum or zinc respectively during deposition. The water is generally known as the oxygen precursor as it deposits the oxygen onto these surfaces.

Both processes go generally as follows: A substrate is placed in an ALD chamber. As a CVD technique, the first step of ALD is to admit one of the gaseous precursors into the chamber. This precursor interacts with the surface. The precursors are chosen that after the initial interaction the surface becomes almost inert to the precursor. Furthermore, the precursor does not react with itself or with any byproducts, namely ethane or methane. These properties deem the chemical reactions self-terminating [10]. The self-terminating nature of these reactions keeps the reactions that must be included in the model to practical amount.

The next step is to purge the chamber of any byproduct, specifically the byproducts ethane or methane and whatever amount of precursor that was not involved in the interaction. This is done with a blast of inert gas, typically argon or nitrogen. Once the chamber is purged, the next precursor can be pulsed into the chamber. This process can be repeated as desired.

1.2.1. ZnO from DEZ and H2O. This technique used to deposit ZnO uses water and DEZ as precursors. The chemical reactions to be studied with this model are summarized below. This section is a summary of the reactions used in Weckman's model [11].

1.2.1.A. The DEZ Pulse and Purge. DEZ is composed of a zinc atom sandwiched between two ethyl ligands in a mutual cis position [26]. The ethyl ligands consist of two carbon atoms, one of these carbon atoms has three hydrogen attached, the other has only two. This carbon atom with two hydrogens is the one attached to the zinc atom.

In the presence of a nearby hydrogen the aforementioned carbon atom can detach from the zinc atom and the entire ligand along with it. The hydrogen can then attach to the carbon atom that is connected to two hydrogens. Thus, the ethyl ligand becomes ethane gas and the remaining zinc atoms with one ligand attached is now called monoethylzinc (MEZ).

During the DEZ pulse the metal precursor will settle on top of water or hydroxyl molecules. The DEZ has a slight chance of desorbing or leaving the surface. If the DEZ molecule remains on the surface in the presence of hydrogen, then one of the ethyl ligands will rob a nearby hydrogen, releasing ethane gas and depositing MEZ onto the surface. It is possible that the MEZ can interact further with hydrogen in the surface to remove the remaining ethyl ligand.

Typically, MEZ will remain on the surface until the end of the DEZ pulse. When the chamber is purged, most of the MEZ remains, and the majority of the chemical purged comes from leftover precursor as well as the gaseous ethane byproduct of this half-cycle. According to Weckman, not much of interest occurs during the purge [11].

1.2.1.B. The Water Pulse and Purge. During the water pulse a similar reaction occurs where the incoming water molecules settle on top of the surface. If the water molecule is near an ethyl ligand it will donate a hydrogen to release ethane gas similar to the DEZ pulse. After the ethyl ligands are removed the zinc undergoes a process called densification where its position shifts slightly as it settles into the ZnO lattice.

As the primary source of free hydrogen, the diffusion of these hydrogens across the surface happens often during this pulse. This event where hydrogens are dispersed across the surface attaching to oxygen atoms to form hydroxyl or water molecules is called proton diffusion. In layman's terms the oxygen atoms play a game of molecular hot potato with the hydrogen atoms.

At the end of the water pulse there ideally will be enough hydrogen on the surface in the form of water or hydroxyl molecules such that the incoming DEZ molecules from the next pulse will have ample opportunity to react with the surface.

1.2.2. Al_2O_3 from TMA and H2O. The chemical reactions for the deposition of Al_2O_3 with TMA and water share many similarities with that of the ZnO deposition discussed earlier. Again, this section summarizes the chemical reactions that Weckman described [13].

Here the TMA is composed of an aluminum atom that is centered between three methyl ligands [12]. These methyl ligands are each made of a single carbon atom with three hydrogens attached.

In a familiar fashion, methyl ligands in the presence of hydrogen will detach from the aluminum and combine with the hydrogen to form methane gas. While the chemical reactions occur similarly, there are three ligands with TMA opposed to the two found in DEZ.

1.2.2.A. The TMA Pulse and Purge. During the TMA pulse, the TMA molecules will settle on top of the surface. The TMA has a chance of desorbing or even translating along the surface of the slab. The TMA attaches in a helicopter fashion. If hydrogen is nearby then one of the methyl ligands will detach from the aluminum atom and combine with the hydrogen to release methane gas from the surface. Like ethane, methane does not interact with the surface, other precursor molecules, or itself [5].

The TMA has now become dimethylaluminum (DMA) and is just an aluminum atom with two methyl ligands. The DMA is situated in mickey mouse fashion with both ligands pointing up and away from each other. DMA can further interact with in the surface hydrogen to form monomethylaluminum (MMA). It is possible for the MMA to also interact with a hydroxyl molecule on the surface to form monomethylaluminum hydroxide (MMA-OH). This MMA-OH

can decompose to aluminum hydroxide. These are the some of the different surface species that can exist. All of these decomposition reactions can occur during the purge as well.

1.2.2.B. The Water Pulse and Purge. Again, the water pulse is the main source of reactive hydrogen. During this pulse the water molecules can settle onto the surface and again donate their hydrogens to ethyl-ligands on the surface. The decomposition of any remaining DMA or MMA can occur in manners similar to those mentioned in the discussion regarding the TMA pulse. Proton diffusion mainly occurs during the water pulse and purge.

1.3. Previous KMC Models

There have been few publications utilizing the KMC method for simulating ALD growth. In 2011, a 2-dimensional KMC framework was presented to model the growth of ZnO nano-wires [29,31]. In 2014, Shirazi et al presented a 3-dimensional KMC framework to model ALD growth of hafnium-oxide (HfO) [10]. Modifying the HfO framework, Weckman et al was able to simulate ZnO ALD growth [11]. The foundations laid by Shirazi and Weckman allow this study to be possible. This section briefly describes the work previously done on this subject.

1.3.1. SPPARKS Model Overview. Shirazi's code utilized a KMC random number generating package called SPPARKS from SANDIA National Laboratory. Feature rich with diagnostic tools, SPPARKS is capable of performing 3d on-lattice KMC simulations. Modularity is also a keyword here as the SPPARKS framework designed was so that it could be modified for various uses including ising models, grain growth, and even atomic layer deposition [14].

Mahdi Shirazi and Simon Elliot created the HfO KMC model which is the sire to the ZnO and now the Al_2O_3 KMC models. A simple summary of the KMC algorithm is as follows: Two random numbers are rolled. The first is used to select an event from an event

list which contains all possible chemical reactions as described in Equation 1. Because of the on-lattice nature of the code, these events occur on a lattice containing many sites. Each event can be thought of as a site changing from one state to another. The second random number is used to calculate the length of the next timestep as described in Equation 2. This process is repeated until the simulation ends ass depicted in Figure 1 [10]. This ability to simulate the time-evolution of systems is what separates the KMC from the traditional Monte Carlo (MC) method which is incapable of doing such a task.

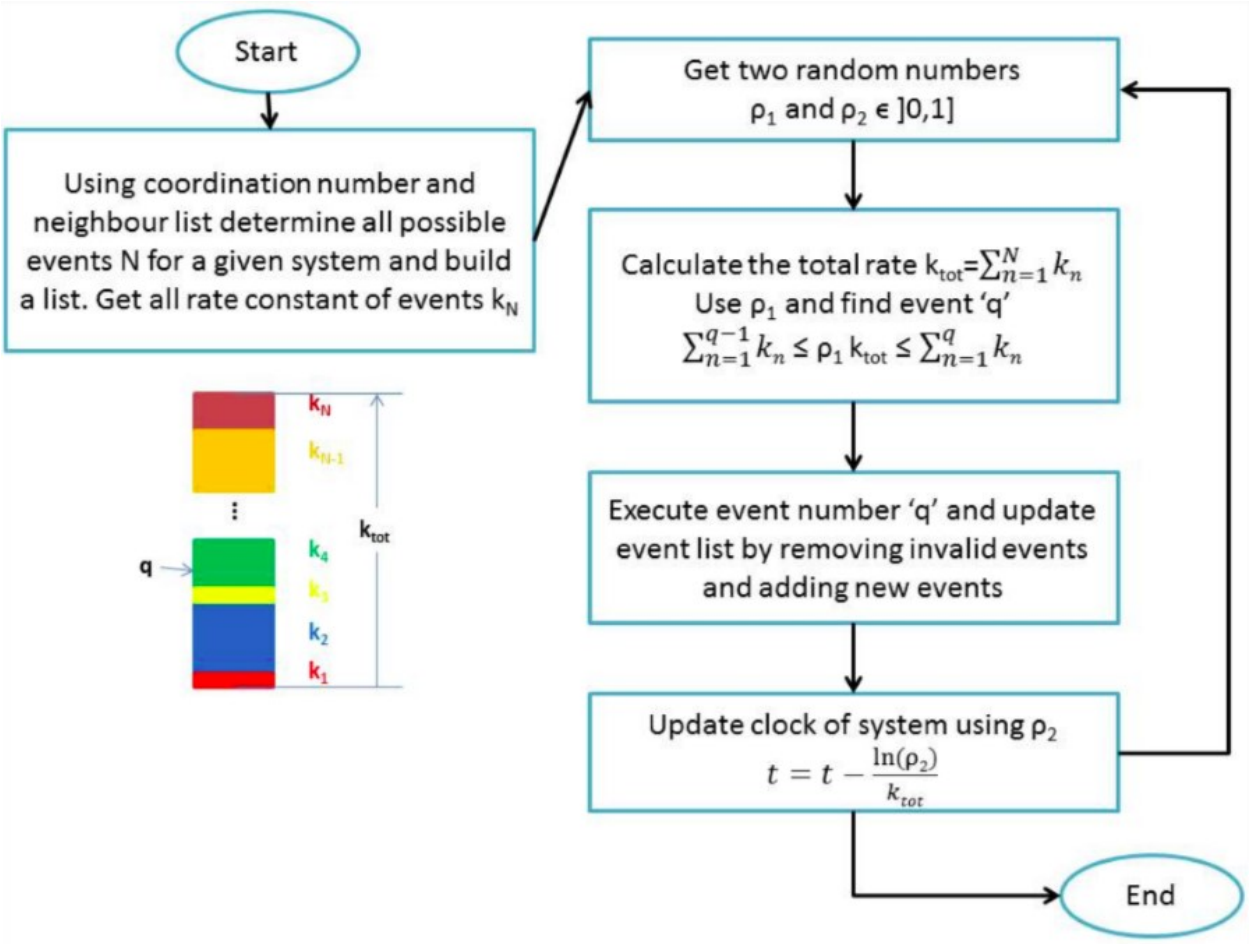

Figure 1. A Flow chart from Mahdi Shirazi's thesis on modeling ALD of HfO with KMC. The chart conveys how the two random numbers generated at each timestep are respectively used to select an event from an event list and update the system clock.

$$\sum_{n=1}^{q-1} k_n \leq k_{total}\rho_1 \leq \sum_{n=1}^{q} k_n \quad \textbf{(Eqtn. 1)}$$

$$\Delta t = \frac{ln\rho_2}{k_{tot}} \quad \textbf{(Eqtn. 2)}$$

1.3.2. Input and Output. It is worth overviewing how the input parameters relate to the data output by the KMC code are related. There are two input files and two output files needed for each simulation. The two input files are the lattice data file and the input script. The lattice data file contains information on the structure and content of the lattice inside the simulation box. The input script contains the reaction list and various adjustable parameters of the simulation.

The two output files are a log file and a dump file. The dump file contains the state of the lattice at each timestep. The relationship between files is depicted in Figure 2 and Figure 3. The log file is more processed and contains graphable information such as mass, population of each molecular species, chemical reaction count, and more.

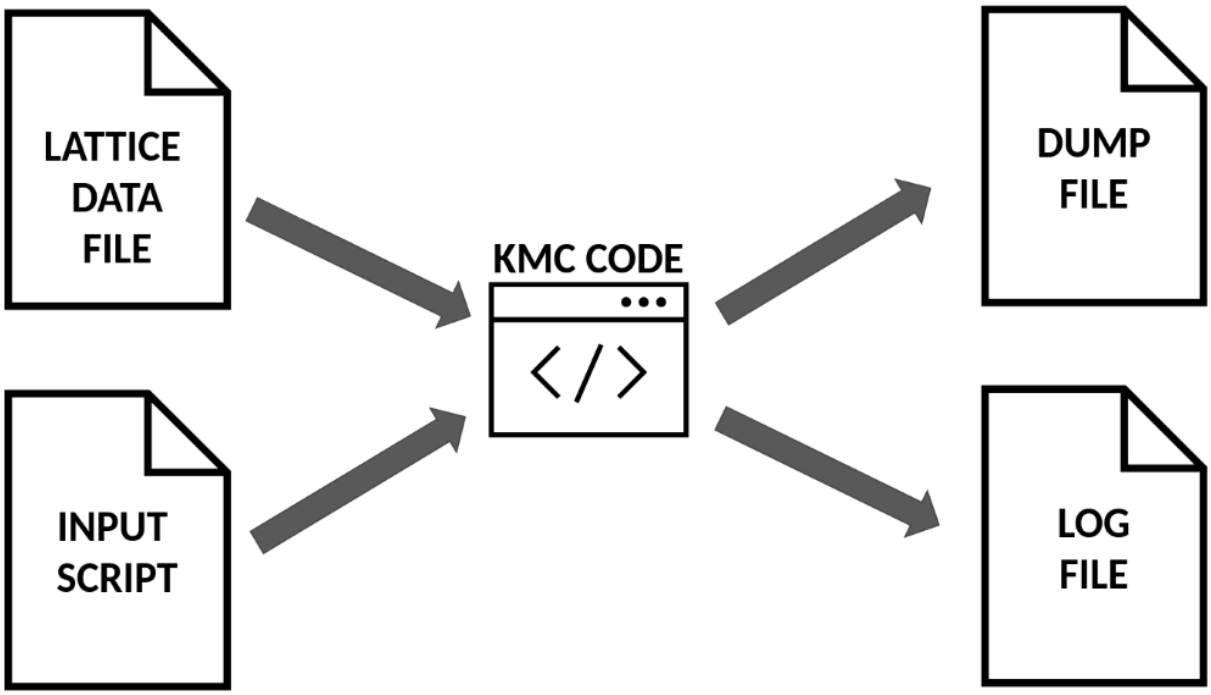

Figure 2. Roadmap of input and output of the SPPARKS KMC code. A diagram conveying the relationship between the different input and output files used by the KMC code.

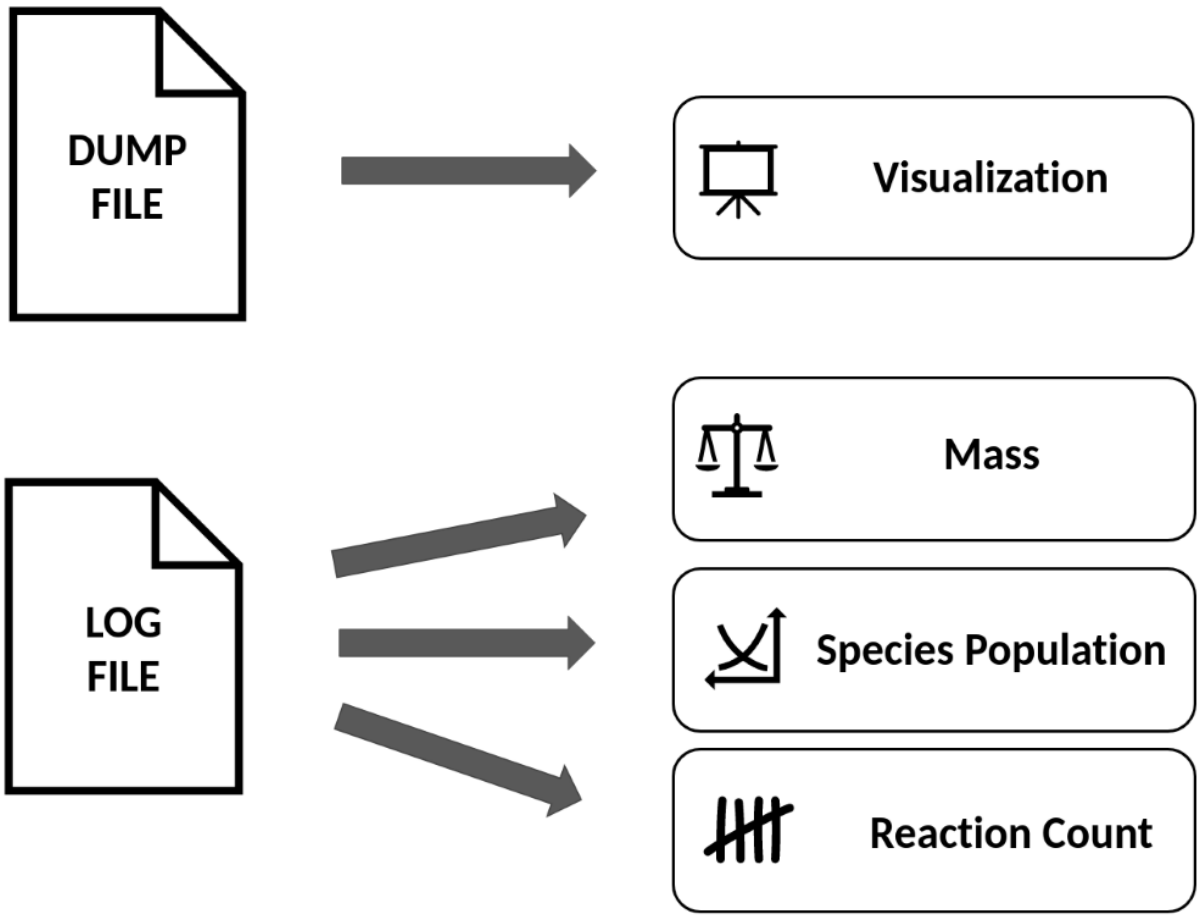

Figure 3. Contents of the SPPARKS KMC output are shown in relation to the output file. A diagram conveying the information contained within the output files of this KMC code.

2. COMPUTATIONAL METHODS

In the last part of the previous section, the general KMC algorithm was overviewed. This section will be dedicated to establishing the computational methods that are used in this study. Since both the existing ZnO and the novel Al_2O_3 models are investigated in this thesis, the best way of explaining both models will be to compare and contrast the two models. This efficiently communicates the properties of both models and how the existing model was modified into a new and separate KMC model.

2.1. The 3D Lattice.

The SPPARKS ALD applications are on-lattice KMC codes. Consider a 3-dimensional grid or lattice inside a region of space called the simulation box. Similar to how chess pieces exist on squares on a chessboard, here molecules are confined to exist in sites on this lattice shown in Figure 4, Figure 5, and Figure 6.

2.1.1. The Ideal Lattice. For two-element substances such as HfO, ZnO, or Al2O3: the lattice is composed of two sub-lattices, one for each element. In the case of ZnO, an oxygen sub-lattice and a zinc sub-lattice exist. At the end of deposition, ideally these sub-lattices will be filled with oxygen and zinc respectively. Likewise, for Al2O3, the sub-lattices would be filled with oxygen and aluminum respectively.

In an ideal ZnO lattice, each site should be connected to four sites in the opposing sub-lattice. That is, every zinc atom will be connected to 4 oxygen atoms and every oxygen atom will be connected to 4 zinc atoms as depicted in Figure 7. Sites with 4 such connections to other sites are deemed to have a coordination number of four [11]. However, for alpha-alumina, the

aluminum sites have a coordination number of six, meaning that these sites have six nearest neighbors [13]. The aluminum atom is depicted in Figure 8 as having a coordination number of six.

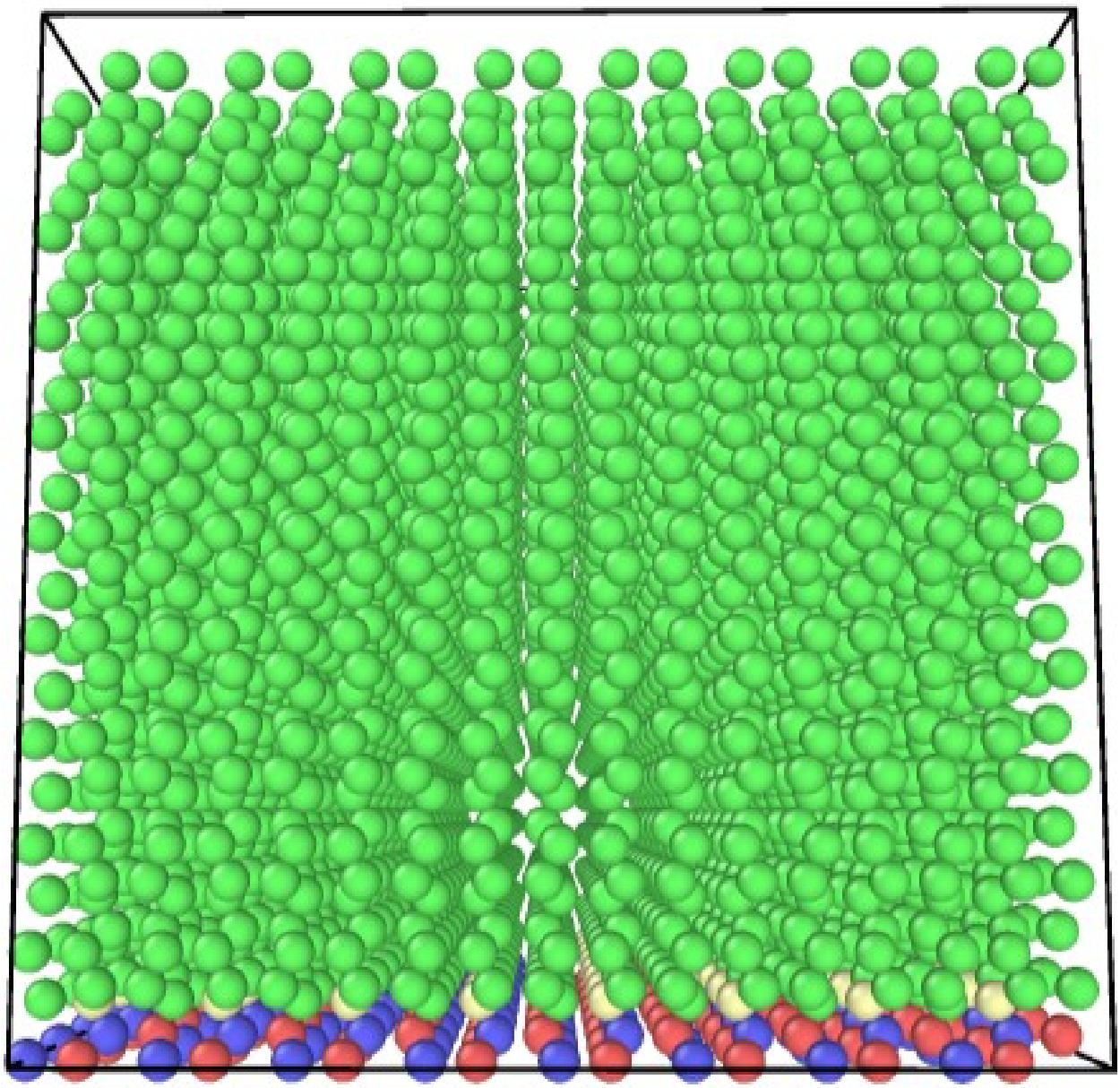

Figure 4. A visualization of the sites that are contained within the simulation box at simulation start. Green spheres represent vacant sites in the lattice, yellow represents water-containing sites, while red and blue represent oxygen and zinc sites.

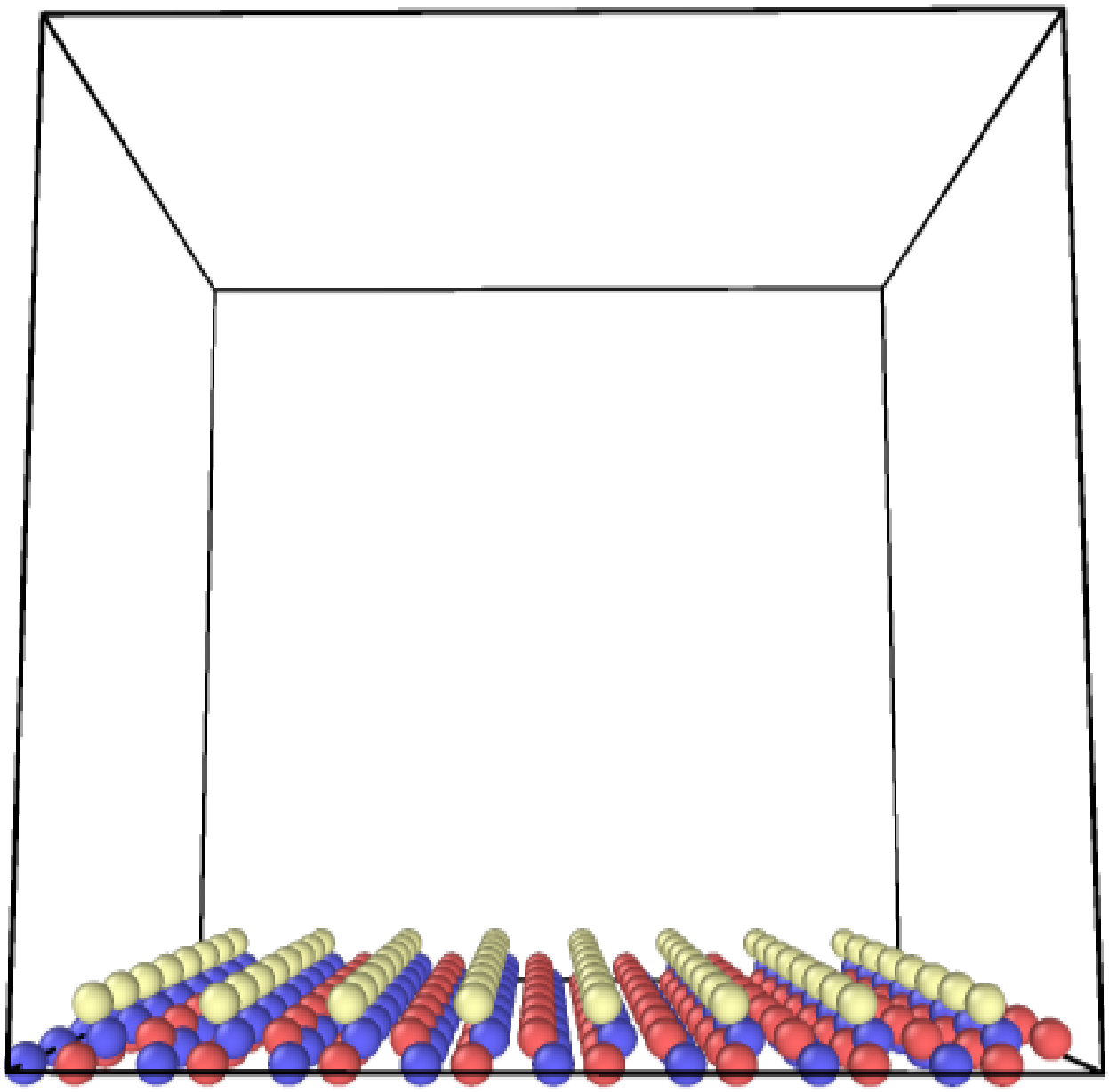

Figure 5. A visualization of the occupied sites that are contained within the simulation box at simulation start. Yellow represents water-containing sites, while red and blue represent oxygen and zinc sites. Vacant sites, previously seen in green, have been removed from this image. This is a site-based depiction of the initial surface for the default ZnO KMC model. As the simulation progresses, more sites will become visible as they become occupied. There are other methods of visualization an each can be chosen depending on whether a sites-based representation or molecular representation is desired.

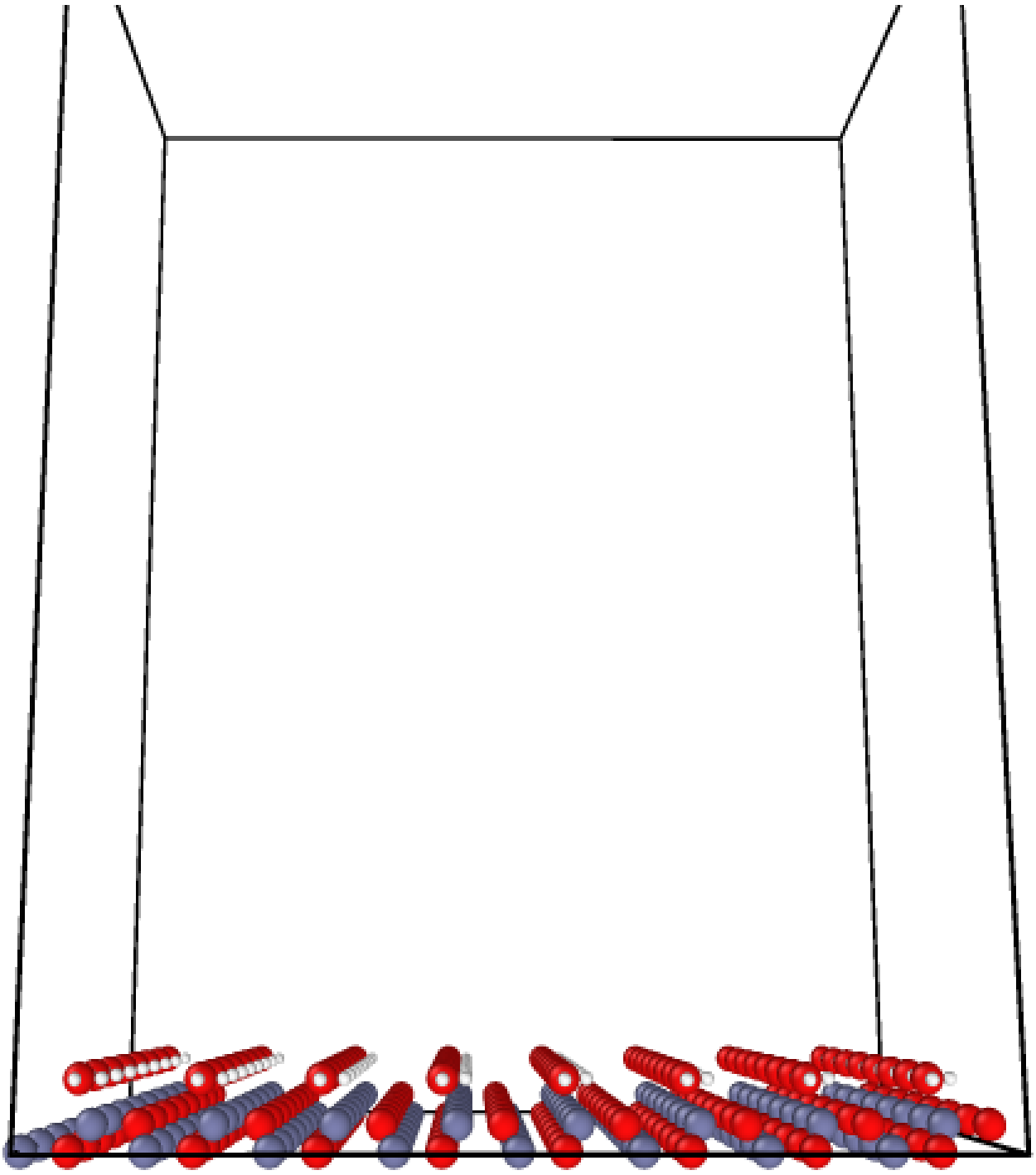

Figure 6. A visualization of the atoms present within the simulation box at simulation start. White spheres represent hydrogen atoms, while red and blue represent oxygen and zinc atoms. This image represents the atomic-based visualization of the initial surface for the default simulation of the ZnO KMC model.

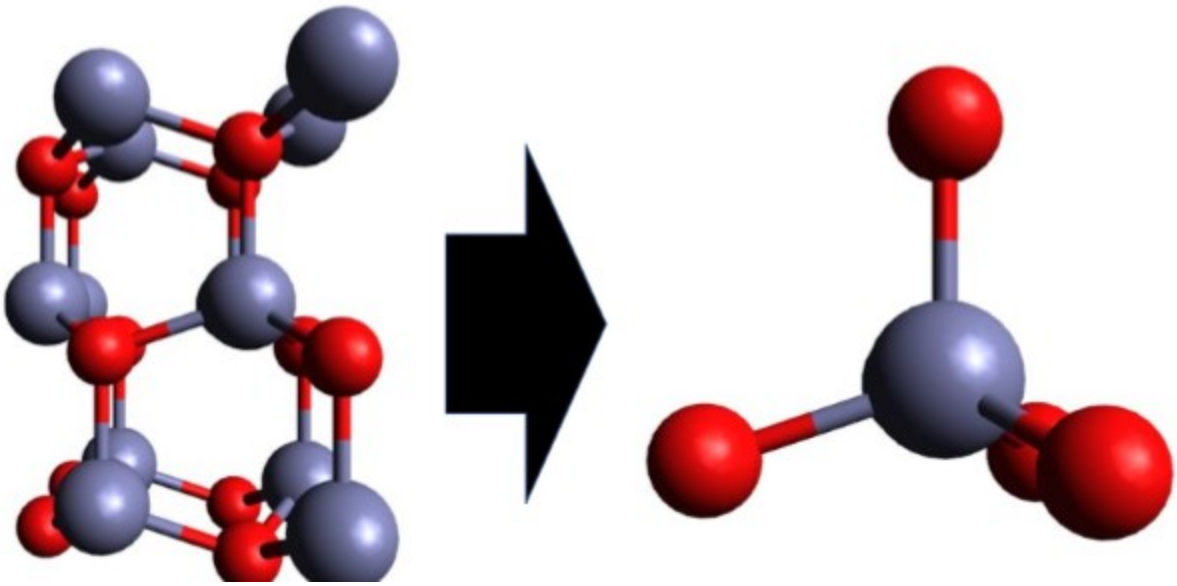

Figure 7. On the left is an excerpt from a hexagonally packed ZnO lattice. On the right is an isolated zinc atom, in blue, connected to four oxygen atoms, shown in red.

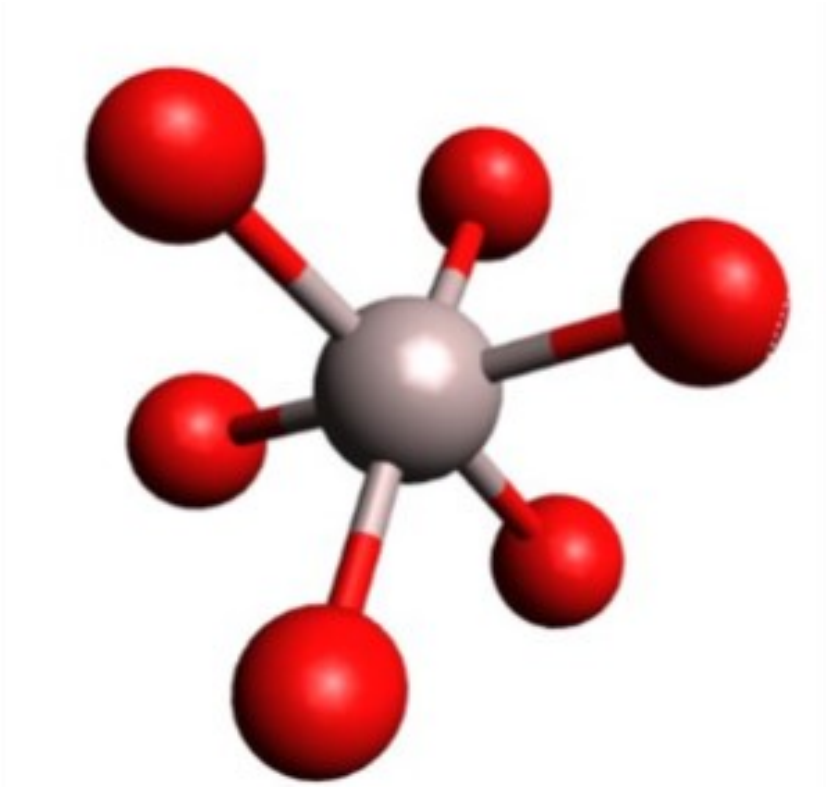

Figure 8. An aluminum atom, shown in pink, is isolated from a lattice of α-alumina. This conveys the maximum coordination number of six for these aluminum sites as they are connected to six oxygen atoms, shown in red.

2.1.2. The Lattice Data File. Computationally speaking, the code reads this lattice information from a lattice data file specified in the input file. Figure 9 shows the lattice data file consists of four parts: a header, a Sites list, a Neighbors list and a Values list. Each of these contains information about the initial surface at simulation start.

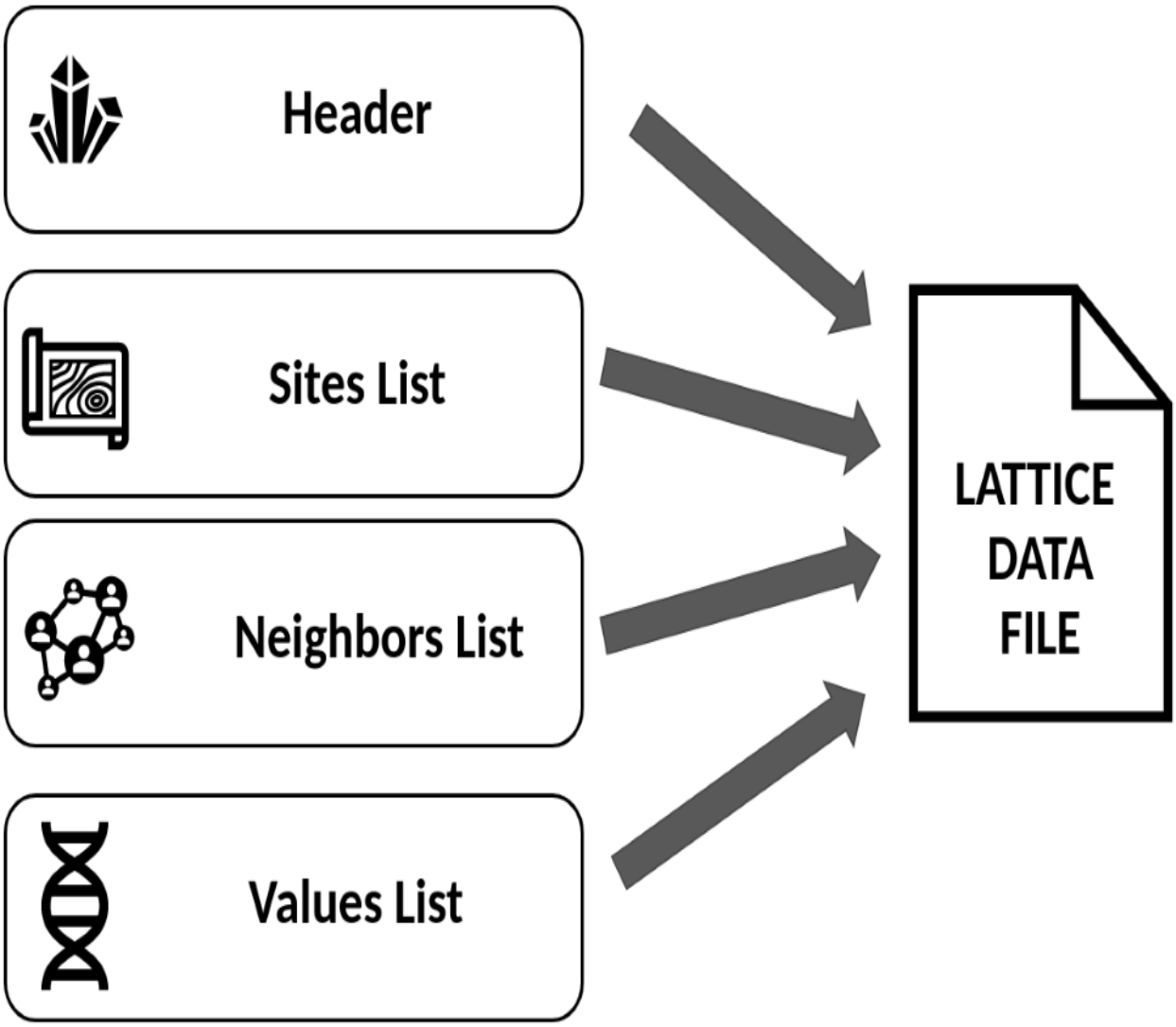

Figure 9. This diagram conveys the information contained within the lattice data file. The header contains information on the geometry of the simulation box. The sites list contains the fractional coordinates of all sites within the simulation box. The neighbors list contains the four nearest neighboring sites, and the values list declares the initial species of every site at simulation start.

The header holds information such as dimensionality, maximum number of nearest neighbors, number of sites, and simulation box size. The dimensionality is set to 3 as this is a 3-dimensional lattice [10]. The simulation box dimensions are set to unity because the site positions are given in the Sites list and are in fractional coordinates.

The Sites list contains a list of site identifiers and their respective positional coordinates. Aside from the visualization and creation of the Neighbor list, the position of each site is irrelevant to the KMC code [10].

The Neighbors list contains a list of the nearest neighbors for each site. In the ZnO code every site has four nearest neighbors [11]. In the Al_2O_3 code, each oxygen site has four nearest neighbors and each aluminum sites has six nearest neighbors. Thus, in the header for A $Al_2O_3$3 lattice data files, the maximum number of nearest neighbors must be set to six.

The Values list contains the initial species and coordination number of every site in the lattice. As such, the surface described by the values list is the initial surface at the beginning of a simulation. For each site in the Values list there is a number indicating the site species and a separate number that indicates the initial coordination of that particular site.

2.1.3. Al_2O_3 Site Species. A list of the possible site species that can appear in the Al_2O_3 simulations presented in this work are listed in Table 1 below. The Species ID column gives a clue that there are plans to incorporate more site species into this code as the reaction list mentioned in the next section becomes more complete.

The site species for Al_2O_3 deposition follow the conventions set in the HfO and ZnO codes. Specifically, the ethyl or methyl groups are replaced by an X. Thus, TMA is represented by AlX3, DMA by AlX2, and MMA by AlX. Table 1 shows only the species used in the chemical reactions currently incorporated into this model.

Table 1. Site Species Included in the Current Al_2O_3 KMC Model

Species ID	Species Name	Species Description
0	VAC	Vacant site.
1	O	Pure oxygen site.
2	OH	Hydroxyl group.
3	OH2	Water molecule.
5	AlX3OH	TMA adsorbed onto Hydroxyl group.
14	Al	Pure aluminum site.
15	AlX2	DMA site.
16	AlX	MMA site.
18	OH2AlX2	Water adsorbed onto DMA.
19	OH2AlX	Water adsorbed onto MMA
20	OHAl	Hydroxyl group on an aluminum atom.
23	OHAlX	Hydroxyl group on a MMA molecule.
24	OAl	Oxygen atom on an aluminum atom.

2.1.4. Morphing Time. One can see from Table 1 that the simulation allows for entire molecules to exist at a site that would only contain a single atom in an ideal lattice. An example would be an entire TMA molecule adsorbed to an OH site to become an AlX3OH site. The entire TMA-OH assembly exists in the same space as oxygen atom is supposed to occupy.

Undoubtedly, this would change the position of the sites nearby and for consequent sites occupied as deposition progresses. This behavior means that Al_2O_3 will grow in a more amorphous manner than this on-lattice model might predict. For the purposes of this work, the effect of variable site positions is neglected and the ideal lattice spacing is maintained throughout any simulation. This could potentially mean that density values computed from this KMC output might be more dense than experimentally recorded values.

Shirazi mentioned the intriguing idea of updating new site positions on-the-fly [10]. Constantly updating the positions of sites in the lattice would increase computational expense. Additionally, the changing geometry of the lattice might affect the values of the energy barriers discussed in the next section.

2.2. The Reaction List.

The reaction list contains all valid reactions that can occur in the KMC system. For this on-lattice code, each reaction consists of which species a given site can convert into. It was previously mentioned that a TMA molecule can adsorb onto an OH site. This is described by reaction RL1 in Table 2 below. No modifications were made to the reaction list from Weckman's code for ZnO reactions [11]. The reaction list for the Al_2O_3 application consists exclusively, but not all-inclusively, of reactions and energy barriers gleaned from Weckman's ab initio study of Al_2O_3 deposition [13]. In the following paragraphs the included chemical reactions that Weckman described are summarized and translated into a reaction list more compatible with the KMC code.

In RL1, the OH site becomes an AlX3OH site. Notice the Site I1 column holds the value of OH and is the initial species of the site. The Site I2 column holds the value of the final species of the aforementioned site. If there is a neighboring site involved during the reaction, the initial and final species of that neighboring site will be listed in the Site J1 and Site J2 columns respectively. Each reaction has an associated energy barrier that defines the energy in electron-Volts required for said reaction to occur. The value of the Cycle column indicates when the reaction may occur in the deposition cycle. To clarify: If the Cycle value is 1, then the reaction only occurs during the metal pulse. If the Cycle is 2, then the reaction only occurs during the water pulse. If the Cycle is set to 0 then the reaction may occur during any pulse or purge.

This reaction list must be declared in the input script according to the format laid out by Shirazi [10]. Table 2 contains energy barrier values that remain constant with varying temperature, pressure, etc. The reactions declared in the input script must also include the appropriate rate coefficients discussed in following section whose values change with these

parameters. It should also be noted that negative energy barriers should be set to zero in the input script to the KMC code. Another important thing to note when working with any of the KMC-ALD applications is that the KMC source code and the reaction list are heavily interdependent. As such, adding reactions to the reaction list may require editions to the source code as well.

Table 2. List of Reactions Included in the Current Al_2O_3 KMC Model

RLID	Site I1	Site I2	Site J1	Site J2	Barrier	Cycle	Notes
RL1	OH	AlX3OH	---	---	-1.13	1	TMA Adsorption
RL2	AlX3OH	OH	OH	AlX3OH	0.88	0	TMA Translation
RL3	AlX3OH	OH	---	---	-1.13	0	TMA Desorption
RL4	AlX3OH	O	VAC	AlX2	0.35	0	1st Lig. Removal
RL5	AlX2	AlX	OH	O	0.51	0	2nd Lig. Removal
RL6	AlX	Al	OH	O	1.05	0	3rd Lig. Removal
RL7	AlX2	OH2AlX2	---	---		2	H2O Ads. DMA
RL8	OH2AlX2	OHAlX	OH	OH	0.44	0	2nd Lig. Removal
RL9	OHAlX	OHAl	VAC	OH		2	Ads MMAOH
RL10	OHAl	Al	VAC	OH	0.67	0	MMAOH Clean
RL11	AlX	OH2AlX	---	---		2	H2O Ads. MMA
RL12	OH2AlX	OHAlX	OH	OH2	1.13	0	Create MMAOH
RL13	OH2AlX2	OHAlX2	OH	OH2	0.26	0	Proton Exchange
RL14	OHAlX	OH2AlX	VAC	OH		2	Ads. MMA #2
RL15	OH2AlX	Al	VAC	OH	0.3	0	Final Removal
RL16	OH2	OH	O	OH	0.6	0	Proton Diffusion
RL17	OH2	OH	OH	OH2	0.6	0	Proton Diffusion
RL18	O	OH	OH	O	0.6	0	Proton Diffusion
RL19	OH	O	O	OH	0.6	0	Proton Diffusion

2.2.1. TMA Pulse Reactions. RL1 occurs during the TMA pulse. The remaining reactions discussed in this subsection may occur at any point in the simulation however they are most likely to occur during the TMA pulse or purge. While TMA is known to be able to adsorb onto other species such as water, oxygen, and aluminum, the adsorption onto OH is currently the only TMA adsorption reaction included in the Al_2O_3 model.

After the adsorption described by RL1, the TMA has a probability of desorbing or possibly translating to a nearby OH site. The reaction list entries for these are RL2 and RL3 respectively. Removal of the first ligand, listed RL4, occurs when the hydrogen from the OH group in the TMA-OH site combines with a ligand to form a methyl group. This methyl molecule is gaseous and does not interact with the surface and is ignored in the simulation. Thus, the original OH site now becomes an O site whilst kicking the remaining DMA molecule into a nearby vacant VAC site. There is a possibility that the second and third methyl ligands can be removed via a reaction with a nearby OH site as described by RL5 and RL6 respectively.

2.2.2. H2O Pulse Reactions. Unlike the singular adsorption reaction listed for TMA, there are four such adsorption reactions that occur during the water pulse summarized in this subsection. One of these adsorption reaction involves the interaction between water and a DMA site. The other three reactions deal with two separate mechanisms by which the third methyl ligand on an MMA can be removed.

Reaction RL7 handles the adsorption of water onto DMA. During RL7, the AlX2 site becomes an OH2AlX2 site. This follows the previously held convention of listing the uppermost molecule first. Another ligand removal is described by RL8. If there is a nearby OH molecule, then 2OHAlX2 can become an OHAlX molecule. The neighboring OH site remains unchanged but the adsorbed onto the DMA becomes an MMA-OH molecule, otherwise known as OHAlX.

The second adsorption reaction to be covered here will be the adsorption of water onto this newly formed MMA-OH site described by R9. In the KMC input this reaction is defined as Site I changing from OHAlX to OHAl while neighboring Site J changes from VAC to OH. In this manner, the adsorbed water molecule archetypally donates a hydrogen to remove the last

methyl ligand and becomes a neighboring OH molecule. In RL10 the OHAl site becomes a pure Al site while kicking the OH to a neighboring site.

The third water adsorption reaction described by RL11 is of water directly adsorbing onto MMA. Unlike previous reactions which were consequent to an adsorption, the RL12 reaction does not remove a methyl-ligand but instead produces the MMA-OH molecule in Site I while forming a separate OH molecule in neighboring Site J.

2.2.3. Proton Diffusion and KMC Pedaling. Reactions RL16 through RL19 all describe sites trading protons between their neighbors. Essentially, the simulation has these sites play atomic hot potato with the hydrogen atoms. Proton diffusion is vital to ALD as it allows for the protons to disburse to sites where they can react. Without this diffusion it is likely that the protons would get trapped in inert sites incapable of interacting with their neighbors. Thus, allowing protons to travel about the surface through this mechanism allows the possibility for more interactions to occur.

There is a computational importance in having seemingly unproductive reactions like proton diffusion, adsorbent translation or desorption. Having reactions such as these in the reaction list decrease the possibility of having an empty reaction list. As mentioned before this empty reaction list can cause a premature termination of the simulation as the program calculates an infinite timestep from Equation 2. Metaphorically, these reactions pedal the program the way one might pedal an accelerator in an unreliable manual transmission vehicle in an attempt to prevent it from dying at idle. The dual necessity of this reaction is described later but to briefly summarize: The physical use of proton diffusion is so that the active hydrogen move to sites where they can be used in a chemical reaction, the computational reason stems from Equation 2.

2.3. Reaction Rate Coefficients.

Each Reaction in the reaction list must have an associated reaction rate coefficient declared in the input script. For each type of ALD, there are three distinct values rate coefficients. Adsorption rate coefficients exist for each adsorbent molecule and there is another rate coefficient that governs the remaining and subsequent surface reactions.

The adsorption rate coefficient follows Equation 3 [10]. K is Boltzmann's constant. P is the chamber pressure in Pascals, m is the kilogram mass of the adsorbent, A is the area of the adsorption site and T is the temperature in Kelvin.

$$K_{Surface} = \frac{h}{k_B T} e^{\frac{\Delta G}{k_B T}} \approx \frac{h}{k_B T} \quad \text{(Eqtn. 3)}$$

The surface rate coefficient can be approximated by Equation 4 below. Thus, the surface rate coefficients are constant with pressure and only dependent upon deposition temperature. These equations come from kinetic gas theory [10].

$$K_{Adsorption} = \frac{\sigma P A}{\sqrt{2 m_{ads} k_B T}} \approx \frac{P A_{Ads}}{\sqrt{2 m_{ads} k_B T}} \quad \text{(Eqtn. 4)}$$

The values of these rate coefficients are like the pressure and temperature knobs for the KMC code. Adjusting these values allows the user to simulate deposition in various combinations of temperature and pressure. Below, Table 3 and Table 4 provide convenient reference for unit conversion of pressure and temperature respectively. In the next sections, rate coefficients will be computed for both ZnO and Al_2O_3 deposition.

Table 3. Handy Units of Pressure

Pressure (Pa)	Pressure (Torr)	Pressure (mBar)	Pressure (Atm)
2	0.015	0.02	1.97E-05
5	0.0375031	0.05	4.93E-05
15	0.112509	0.15	1.48E-04
20	0.15	0.20	1.97E-04
266	2	2.66	2.62E-03
101325	760	1013.25	1E00

Table 4. Handy Units of Temperature

Temperature (K)	Temperature (C)	Temperature (eV)
300	26.85	0.02585
325	51.85	0.02801
330	56.85	0.02844
335	61.85	0.02887
340	66.85	0.02930
350	76.85	0.03016
375	101.85	0.03231
400	126.85	0.03447
425	151.85	0.03662
450	176.85	0.03878

2.3.1. Rate Coefficients for Al_2O_3. The simplest rate coefficients to compute are the rates for surface reactions. Since the only variable in Equation 4 is temperature, these values should be valid for both Al_2O_3 and ZnO surface reaction rates. These surface reaction rates are computed in Table 5 for convenient reference. Table 6 depicts the mass and adsoption area of each adsorbant molecule. Table 7 shows the rate coefficients for the water pulse.

It is clear from Equation 3 that the adsorption reaction rate is dependent upon the adsorbent mass and the adsorption area. These parameters are different for Al_2O_3 and ZnO simulations. For Al_2O_3, the aforementioned constants are listed below. The adsorption areas are taken from literature [13]. The adsorbant masses are listed in atomic mass

units. Reaction rates are assigned for each chemical reaction in the reaction list. The reaction list is declared in the input script to the KMC code. This relationship between the reaction list and the input script is depicted in later on in Figure 10. The reaction rates also control pressure and temperature for the simulation.

Table 5. Rate Coefficients for TMA Adsorption

Temperature (K)	Pressure 2 Pa (Hz)	Pressure 5 Pa (Hz)	Pressure 15 Pa (Hz)	Pressure 20 Pa (Hz)	Pressure 226 Pa (Hz)	Pressure 101325 Pa (Hz)
300	7.19E+12	1.80E+13	5.40E+13	7.19E+13	9.57E+14	3.65E+17
325	6.91E+12	1.73E+13	5.18E+13	6.91E+13	9.19E+14	3.50E+17
350	6.66E+12	1.67E+13	5.00E+13	6.66E+13	8.86E+14	3.37E+17
375	6.44E+12	1.61E+13	4.83E+13	6.44E+13	8.56E+14	3.26E+17
400	6.23E+12	1.56E+13	4.67E+13	6.23E+13	8.29E+14	3.16E+17
425	6.04E+12	1.51E+13	4.53E+13	6.04E+13	8.04E+14	3.06E+17
450	5.87E+12	1.47E+13	4.41E+13	5.87E+13	7.81E+14	2.98E+17

Table 6. Mass and Area of Al_2O_3 Adsorption Precursors

Adsorbant Species	Mass (AMU)	Adsorption Area (nm^2)
TMA	72.10	0.2000 [13]
H2O	18.02	0.2008 [13]

Table 7. Rate Coefficients for H2O Adsorption for Al_2O_3

Temperature (K)	Pressure 2 Pa (Hz)	Pressure 5 Pa (Hz)	Pressure 15 Pa (Hz)	Pressure 20 Pa (Hz)	Pressure 226 Pa (Hz)	Pressure 101325 Pa (Hz)
300	1.43E+13	3.58E+13	1.08E+14	1.43E+14	1.91E+15	7.26E+17
325	1.38E+13	3.44E+13	1.03E+14	1.38E+14	1.83E+15	6.98E+17
350	1.33E+13	3.32E+13	9.95E+13	1.33E+14	1.76E+15	6.72E+17
375	1.28E+13	3.21E+13	9.62E+13	1.28E+14	1.71E+15	6.50E+17
400	1.24E+13	3.10E+13	9.31E+13	1.24E+14	1.65E+15	6.29E+17
425	1.20E+13	3.01E+13	9.03E+13	1.20E+14	1.60E+15	6.10E+17
450	1.17E+13	2.93E+13	8.78E+13	1.17E+14	1.56E+15	5.93E+17

2.3.2. Rate Coefficients for ZnO. Using the same equations as for Al_2O_3, the ZnO rate coefficients are listed below for water pulse reactions, metal pulse reactions, and for reactions that occur on the surface of the material. These values are typically on the same order as for Al_2O_3 reaction rates. This make sense as the only two constants that are different between the materials are that of the adsorption site area and of the adsorbant molecule mass as seen in Table 8. Rate coefficients for ZnO deposition are listed in Table 9, Table 10, and Table 11.

Multiple physical parameters of the simulation can be affected by simply updating the reaction rate coefficient which is a variable dependent upon those parameters. It should always be remembered to update the temperature variable in the input script in addition to updating the reaction rates for a new temperature of deposition.

Table 8. Mass and Area of ZnO Adsorption Precursors

Adsorbant Species	Mass (AMU)	Adsorption Area (nm^2)
DEZ	123.5	0.18 [11]
H2O	18.02	0.14 [11]

Table 9. Rate Coefficients for H2O Adsorption for ZnO

Temperature (K)	Pressure 2 Pa (Hz)	Pressure 5 Pa (Hz)	Pressure 15 Pa (Hz)	Pressure 20 Pa (Hz)	Pressure 226 Pa (Hz)	Pressure 101325 Pa (Hz)
300	1.00E+04	2.51E+04	7.53E+04	1.00E+05	1.33E+06	5.08E+08
325	9.64E+03	2.41E+04	7.23E+04	9.64E+04	1.28E+06	4.88E+08
350	9.29E+03	2.32E+04	6.97E+04	9.29E+04	1.24E+06	4.71E+08
375	8.97E+03	2.24E+04	6.73E+04	8.97E+04	1.19E+06	4.55E+08
400	8.69E+03	2.17E+04	6.52E+04	8.69E+04	1.16E+06	4.40E+08
425	8.43E+03	2.11E+04	6.32E+04	8.43E+04	1.12E+06	4.27E+08
450	8.19E+03	2.05E+04	6.14E+04	8.19E+04	1.09E+06	4.15E+08

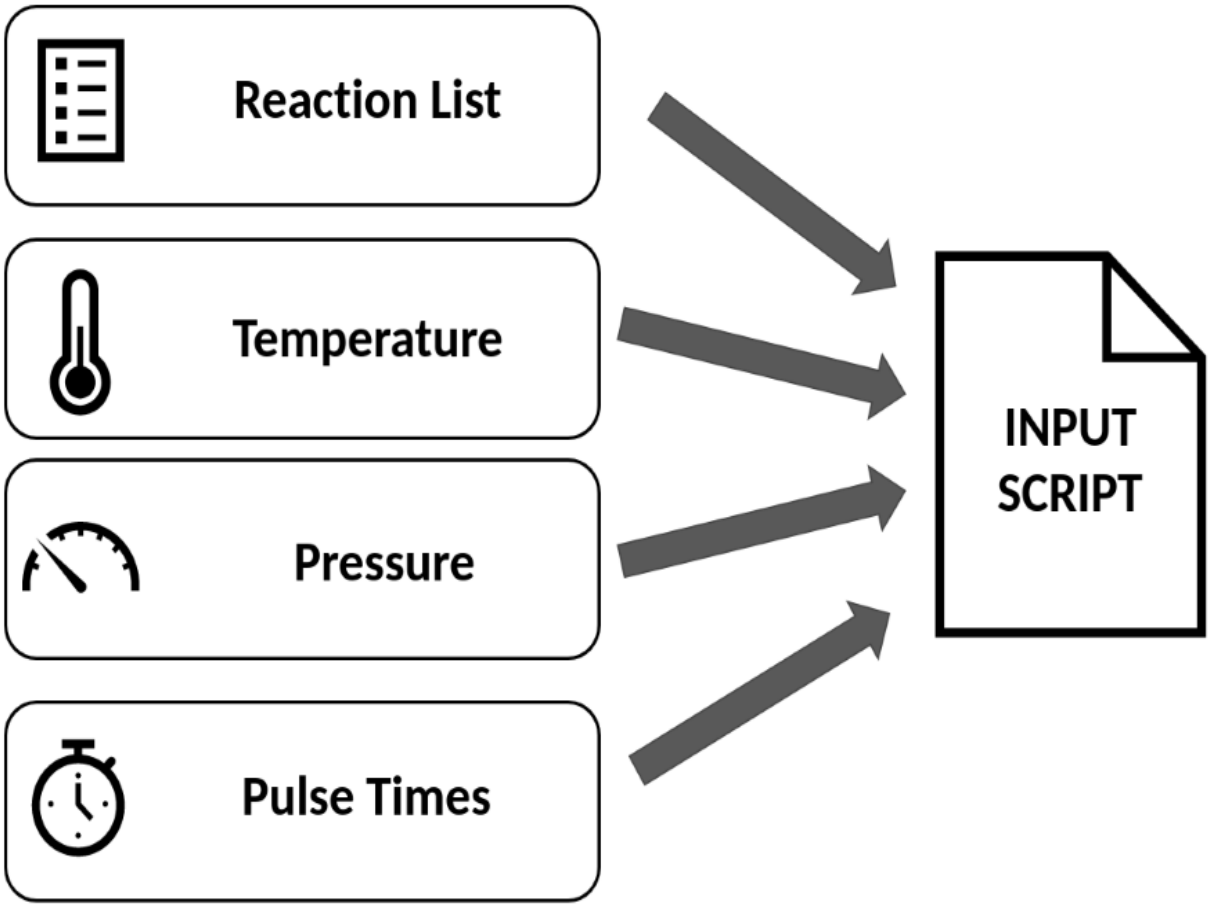

Figure 10. This diagram shows the parameters contained within the input script. Pressure and temperature can be controlled by altering the rate coefficients for each reaction. When changing temperature there is also a temperature parameter that must be updated.

Table 10. Rate Coefficients for DEZ Adsorption

Temperature (K)	Pressure 2 Pa (Hz)	Pressure 5 Pa (Hz)	Pressure 15 Pa (Hz)	Pressure 20 Pa (Hz)	Pressure 226 Pa (Hz)	Pressure 101325 Pa (Hz)
300	4.93E+3	1.23E+04	3.70E+04	4.93E+04	6.55E+05	2.50E+08
325	4.73E+3	1.18E+04	3.55E+04	4.73E+04	6.30E+05	2.40E+08
350	4.56E+3	1.14E+04	3.42E+04	4.56E+04	6.07E+05	2.31E+08
375	4.41E+3	1.10E+04	3.31E+04	4.41E+04	5.86E+05	2.23E+08
400	4.27E+3	1.07E+04	3.20E+04	4.27E+04	5.68E+05	2.16E+08
425	4.14E+3	1.04E+04	3.11E+04	4.14E+04	5.51E+05	2.10E+08
450	4.02E+3	1.01E+04	3.02E+04	4.02E+04	5.35E+05	2.04E+08

Table 11. Rate Coefficients for Surface Reactions

Temperature (K)	Reaction Rate (Hz)
300	6.25E+12
325	6.77E+12
350	7.29E+12
375	7.81E+12
400	8.33E+12
425	8.86E+12
450	9.38E+12

2.4. Reaction Energy Barriers.

This code conserves energy in adherence with the First Law of Thermodynamics. Each reaction in the reaction list has an associated energy barrier. This is the energy required from the system for the reaction to occur. If the system does not have enough energy for a reaction to occur then the reaction will not occur because it will not be found in the updated event list. The conservation of energy is important to this model.

The energy barrier for each reaction can be found by subtracting the energy of the system after the reaction from the energy of the system before reaction. The energy of the system before the reaction can be determined by finding the energy of an isolated precursor molecule and adding it to the energy of a bare surface slab. The energy of the system after the reaction is just the energy of the slab with the precursor molecule adsorbed. Thus, three separate Density Functional Theory calculations are needed for each reaction in the reaction list; one for the isolated precursor, one for the bare surface, and one for the surface with the precursor adsorbed.

$$E_{Barrier} = E_{Slab+Ads} - E_{Slab} - E_{Ads} \quad \text{(Eqtn. 5)}$$

2.4.1. GPAW. The energy barriers used in this work were calculated by Weckman using GPAW. GPAW is a python library that uses C backends capable of performing DFT calculations. Software packages such as VASP and Quantum Espresso perform similar computations [8].

GPAW is named after the Projector Augmented Wave (PAW) method that is used to simplify DFT calculations. These type of DFT
codes perform Self Consistent Field (SCF) calculations. The algorithm is as follows: An initial guess is made for the electron density n. This n is used to calculate and effective field potential which is then used to solve a set of Kohn-Sham equations. These Kohn-Sham equations are a simplified version of Schrodinger's Equation that describe a single electron. From this, the electron density is recalculated and compared with the initial guess. If there is a discrepancy, the process begins again. However, if the values match, then the SCF calculations are complete and now the energies, forces, and geometry can be computed [15]. A visual representation of this can be seen in Figure 11.

2.4.2. DFT Calculations of Molecular Precursors. The easiest type of energies to calculate are those of the single molecules. The specific parameters used for these energy barrier calculations are described by Weckman. To summarize, the molecule is centered in a non-periodic cell with an ample distance of 10 Angstroms between the molecule and the walls of the cell. A PBE functional was used to represent the potential inside the simulation cell [13]. The optimized geometry are compared to accepted values to ensure optimization was properly achieved as shown in Table 12. Similar information is listed for DEZ and TMA in Table 13 and Table 14.

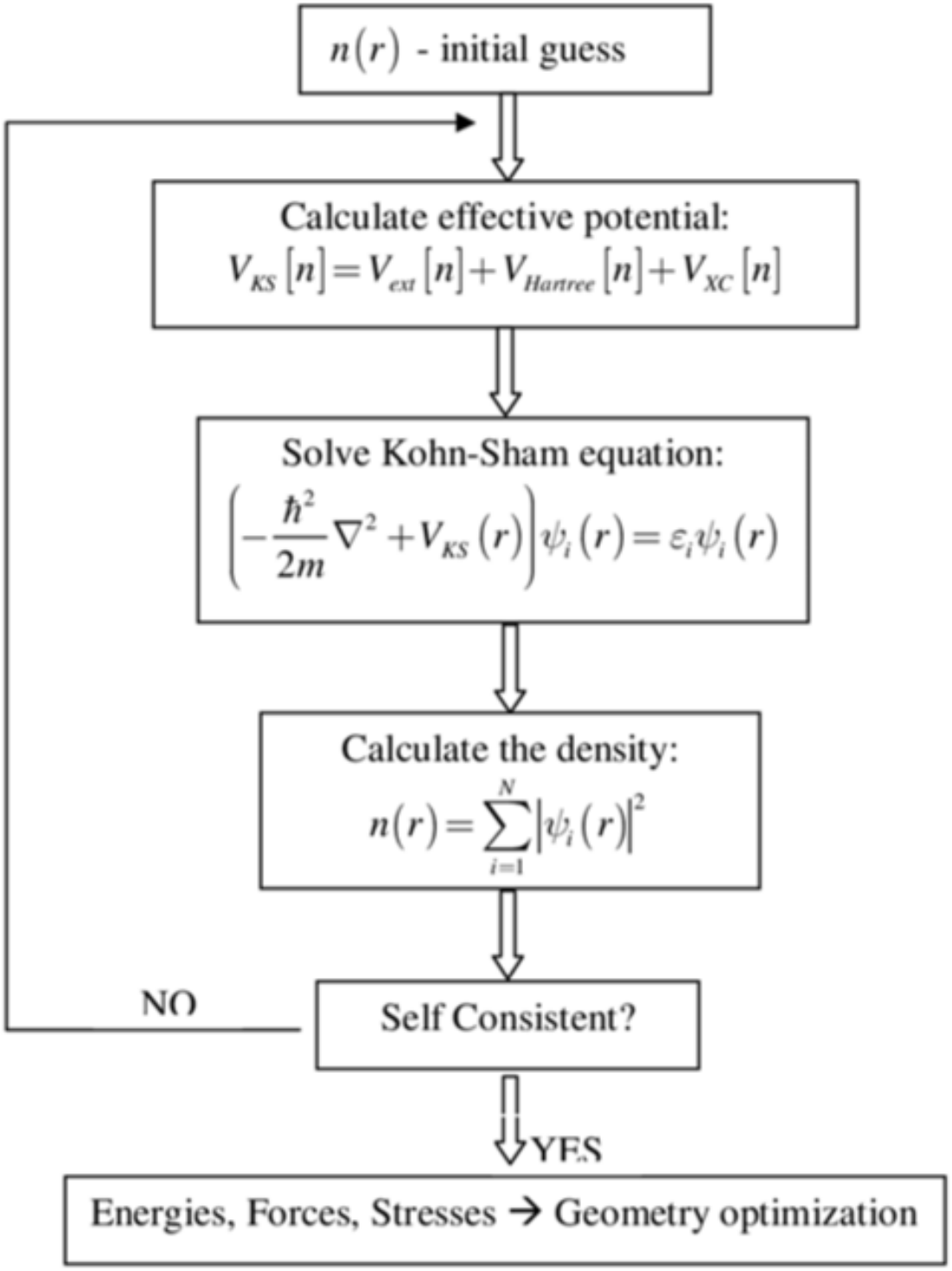

Figure 11. A flow chart demonstrating the algorithm for an SCF calculation. First an initial guess is made for the electron density which is used to calculate an effective potential which is in turn used to solve a set of Kohn-Sham equations. The solution to the one electron approximations of Schrodinger's equation are then finally used to produce the electron density, which if matches with the initial guess, is called self-consistent [16].

2.4.2.A. Optimization of a Water Molecule. An example was found on the GPAW website to optimize the geometry of a water molecule [15]. This example serves as the template for the remaining molecular DFT calculations. The geometry of the relaxed water molecule falls within the accepted range of values for the O-H bond length and the H-O-H bond angle as observed in Figure 12 below.

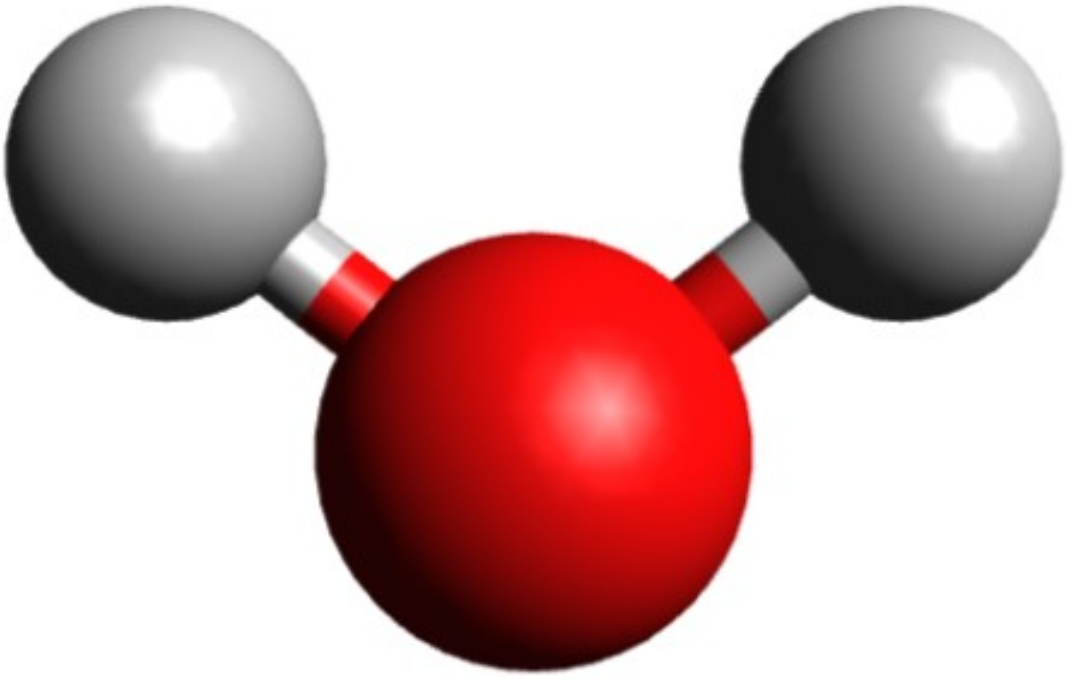

Figure 12. A water molecule represented by one oxygen atom in red and two hydrogen atoms in white.

Table 12. Comparison of Accepted Bond Lengths and Angles of H2O to DFT Calculations

	O-H Bond Length (Angstroms)	H-O-H Bond < (Degrees)
GPAW Computed Values	0.971	103.9
Accepted DFT Values [28]	0.930-0.989	96.4-112.8
Accepted Experimental Values [25]	0.9578	104.9

2.4.2.B. Optimization of The Metal Precursors. Modifying the GPAW example script for water to handle other molecules is straight forward. The only change that needs to be made is to replace the file containing the positions and species of each atom in the molecule. These metal precursor molecules take a slightly longer time to calculate since they contain more atoms.

Again, a close match was found between the optimized geometry and the accepted geometry of the DEZ molecule. It should be noted that there are two versions of DEZ. One exists with the ligands in a mutual cis position as shown in Figure 13 below. The mutual cis position is the more stable geometry for this molecule. The stable geometry of TMA is shown in Figure 14.

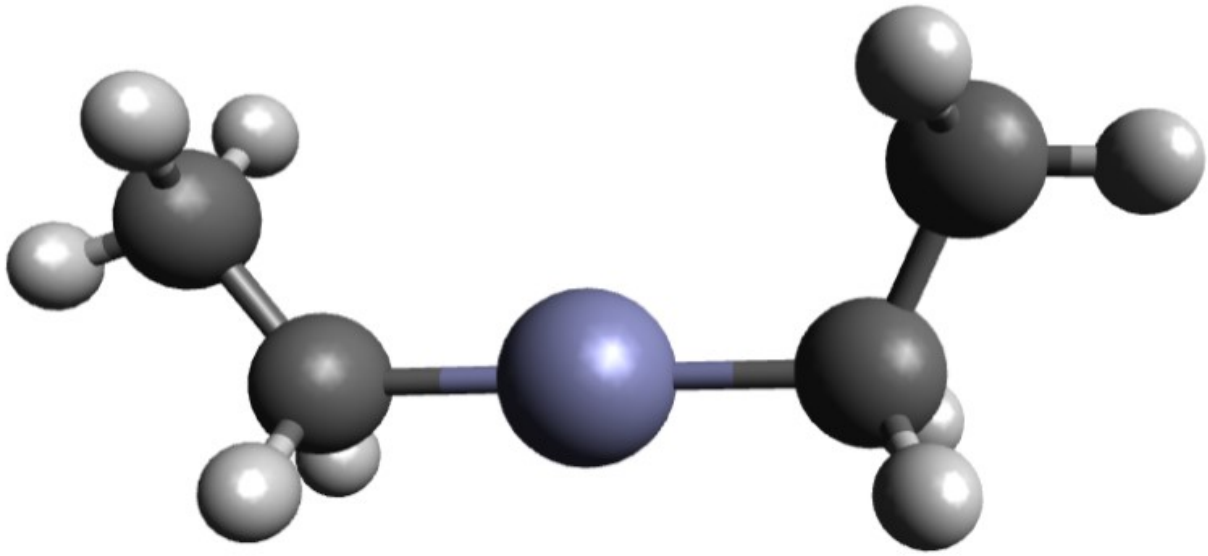

Figure 13. A DEZ molecule represented by zinc in blue, Carbon in gray, and hydrogen in white.

Table 13. Comparison of Accepted Bond Lengths and Angles of DEZ to DFT Calculations

	Zn-C Length (Angstroms)	C-Zn-C < (Degrees)	C-C Length (Angstroms)	Zn-C-C < (Degrees)	C-H Length (Angstroms)
GPAW Computed Value	1.948	177.1	1.537	114.9	1.102
Accepted Value [26]	1.948	176.2	---	115.9	---

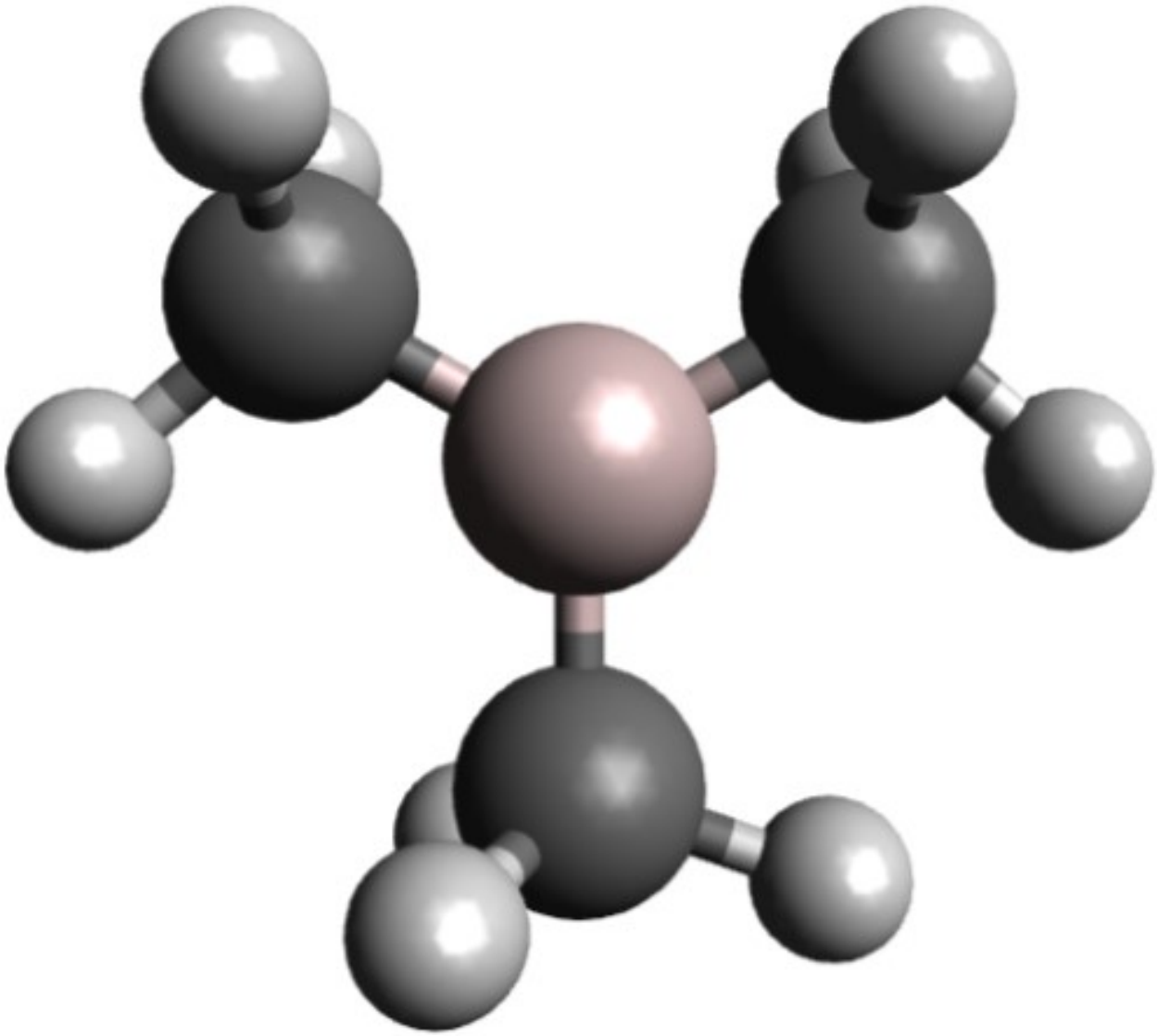

Figure 14. A TMA molecule represented by aluminum in pink, Carbon in gray, and hydrogen in white.

Table 14. Comparison of Accepted Bond Lengths and Angles of TMA to DFT Calculations

	Al-C Length (Angstroms)	C-Al-C < (Degrees)	C-H Length (Angstroms)
GPAW Computed Value	1.974	119.8	1.101
Accepted Value [27]	1.975	119.9	10.098

2.4.2.C. Bare Slab DFT Calculations. Now the optimization of a slab is discussed. First a Crystallographic Information File (CIF) must be created. This can be done by downloading the CIF for a unit cell of the desired material. This unit cell can then be transformed into a super cell using software such as Avogadro. It is important to mind the number of atoms in the slab. Modern computational studies using DFT can at most handle a hundred or so atoms. Even more than a dozen atoms can cause the simulation to take hours to complete.

There are a still a few more modifications that need to be made to the previous GPAW script for single molecules. For slab calculations, the periodic boundary condition must be enabled. Furthermore, in an effort to save computation time, only the uppermost atoms in the slab are allowed to move during relaxation. This is achieved through the use of a masking function which fixes the position of indicated atoms. While there is no vacuum set between the slab and the walls of the simulation, there is a 10 Angstrom vacuum above the slab [15]. Due the periodic nature of slab calculations, there is in effect another slab every 10 Angstroms above the one defined in the script.

2.4.2.D. Slab with Adsorbant Molecule DFT Calculations. The last optimization to be discussed is the optimization of the slab together with the adsorbant molecules on top. Here the script from bare slab calculations will do just fine without any modification. The only difference is that the geometry of the slab now includes the adsorbent molecule in the DFT calculations. This begs the question of where the precursor molecule should be placed. The accepted rule of thumb is to place the molecule to be adsorbed approximately two angstroms above a valid adsorption site [13]. A valid adsorption site is the location of where the atom will eventually settle as adsorption occurs.

2.5. Coordination Numbers.

The HfO and ZnO codes continually track the coordination number of each site. After each event occurs at a particular site, the coordination number of that site and the neighboring sites are updated. The purpose of tracking the coordination number is to incorporate the effect of steric hindrance into the simulation.

Steric hindrance occurs when a cluster of sites becomes crowded with ligands. The more ligands in the area the harder it is to adsorb more DEZ. This is because the energy barrier for this type of reaction increases as the surface density of ligands increases. Thus, a site with a coordination number that indicated crowding will have a higher energy barrier for this reaction in the reaction list.

The Al_2O_3 code does not track the coordination numbers of each site. Instead, it will adsorption interactions as if they occur at low TMA surface coverages. Lower surface coverage, or cases where there is only one DEZ per every 0.18 nm^2, in ZnO ALD leads to a lower barrier for the DEZ adsorption [11]. For low-coverage cases in Alumina, the energy barriers for adsorption are actually higher than high-coverage cases [13]. Though high TMA coverage yields a higher barrier for ligand removal and effectively should dampen growth. These coordination numbers therefore act as another index to sort reactions based on how high their coordination number are and more specifically how many ligands surround the site of interest.

2.6. Seeds and the Stochastic Nature of KMC.

Due to the stochastic nature of KMC simulations, it is necessary to run multiple simulations with identical parameters save for the seed number for the KMC random number generator, which must be different. This is the computational equivalent of running multiple

experiments an averaging the data to mitigate the effect of random “error”. While the KMC code itself is not capable of parallel computation, it is possible to utilize parallel computing to run several identical simulations with various seed values for the KMC random number generator.

2.7. The Terminal Condition.

From Equation 2 it is apparent that when the event list is empty the total of the rate coefficients goes to null and the size of the timestep approaches infinity. Thus, when the surface has exhausted all possible chemical reactions and the surface becomes inert, the simulation jumps to the last time step. This would be as if all chemical reactions ceased after this point in the deposition process. However, this is not a realistic scenario because here there are pulse and purge cycles where chemical reactions are being added. However, because the timestep became too large and jumped past these cycles as demonstrated in Figure 15, the simulation ignores these possibilities.

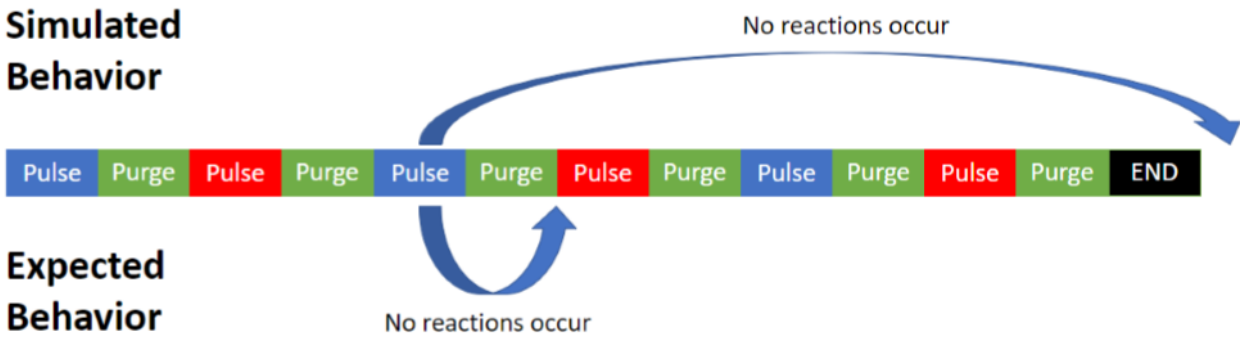

Figure 15. This timeline contrasts what happens during the terminal condition in simulation versus experiment. When no reactions are available, reactions stop until the next pulse or purge when new reactions become available. However, simulations where no chemical reactions are available produce a timestep larger than the entire run of the simulation due to Equation 2.

3. SIMULATION PARAMETERS AND RESULTS

Presented separately in this section, are the parameters and results of several computational experiments involving the two types of ALD of interest. ZnO results will be presented first as these experiments were carried out to ensure proper usage of the KMC method. The method was then extended to allow modeling of Al_2O_3 in a similar though less sophisticated manner. While the previous chapter discussed the general workings of the KMC models, this section will describe a set of experiments as well as their respective parameters and results.

3.1. ZnO Simulations

Unless otherwise specified, the ZnO simulations were conducted per the default simulation parameters used by Weckman [11]. These default parameters call for the use of a 5120-site lattice, with dimensions in Table 15 below. The default pressure is 20 Pa and the default temperature is 400 K. Pulse and purge times were 0.7 seconds and 0.1 seconds respectively for both precursor half-cycles. The input scripts used were all modified version of the ZnO example script. This default script serves as the starting point for all ZnO simulations and the following simulations were all adapted from this template. Snapshots of this simulation taken at simulation start, after eight cycles, and after 16 cycles are shown in Figure 16, Figure 17, and Figure 18 respectively.

Table 15. Dimensions of the Default ZnO Simulation Box

	A (Angstroms)	B (Angstroms)	C (Angstroms)
Length	26.80	41.65	58.02

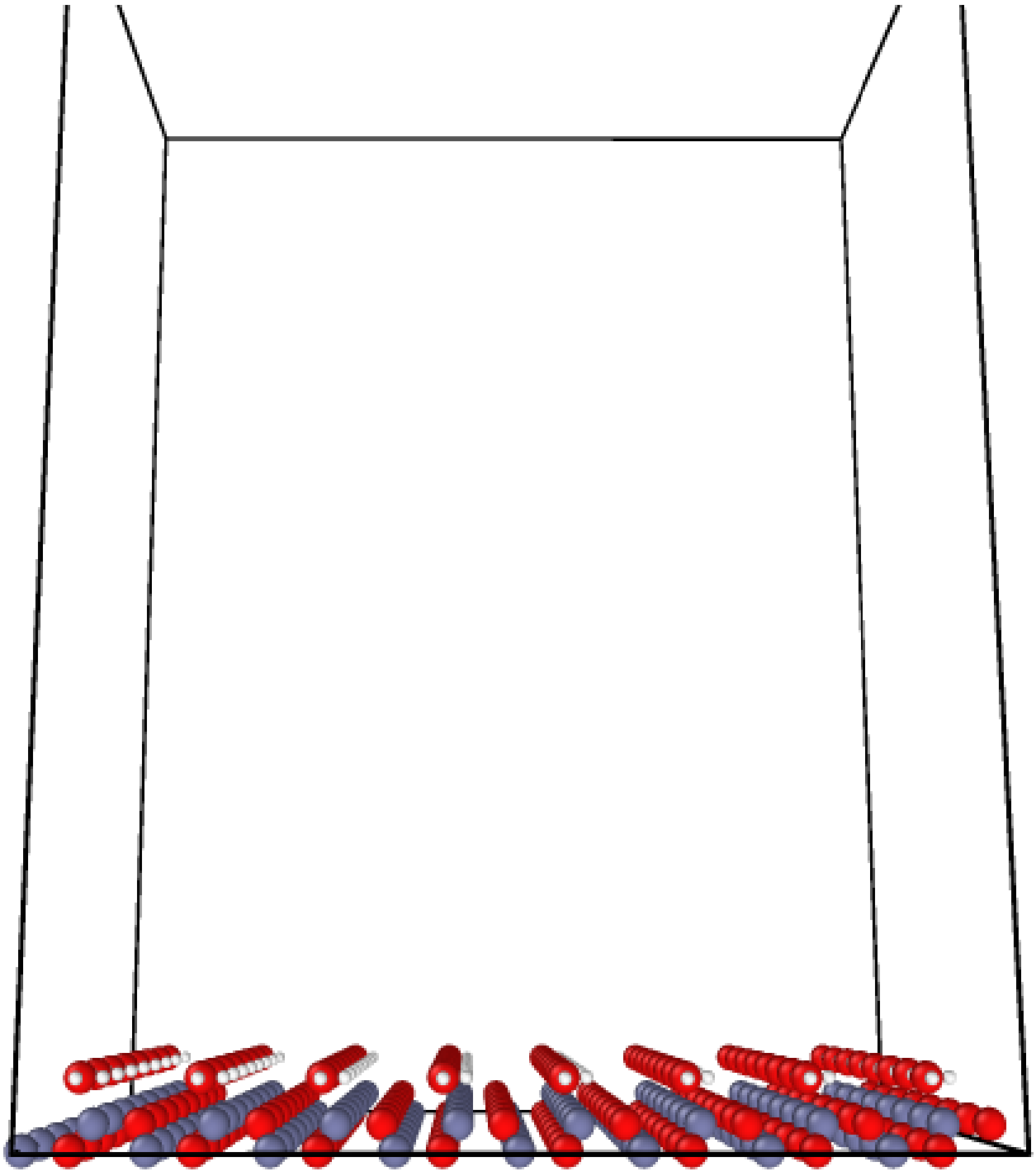

Figure 16. This image depicts the simulation box at simulation start. The zinc, oxygen, and hydrogen atoms represented in blue, red, and white respectively. This shows a ZnO surface covered with water.

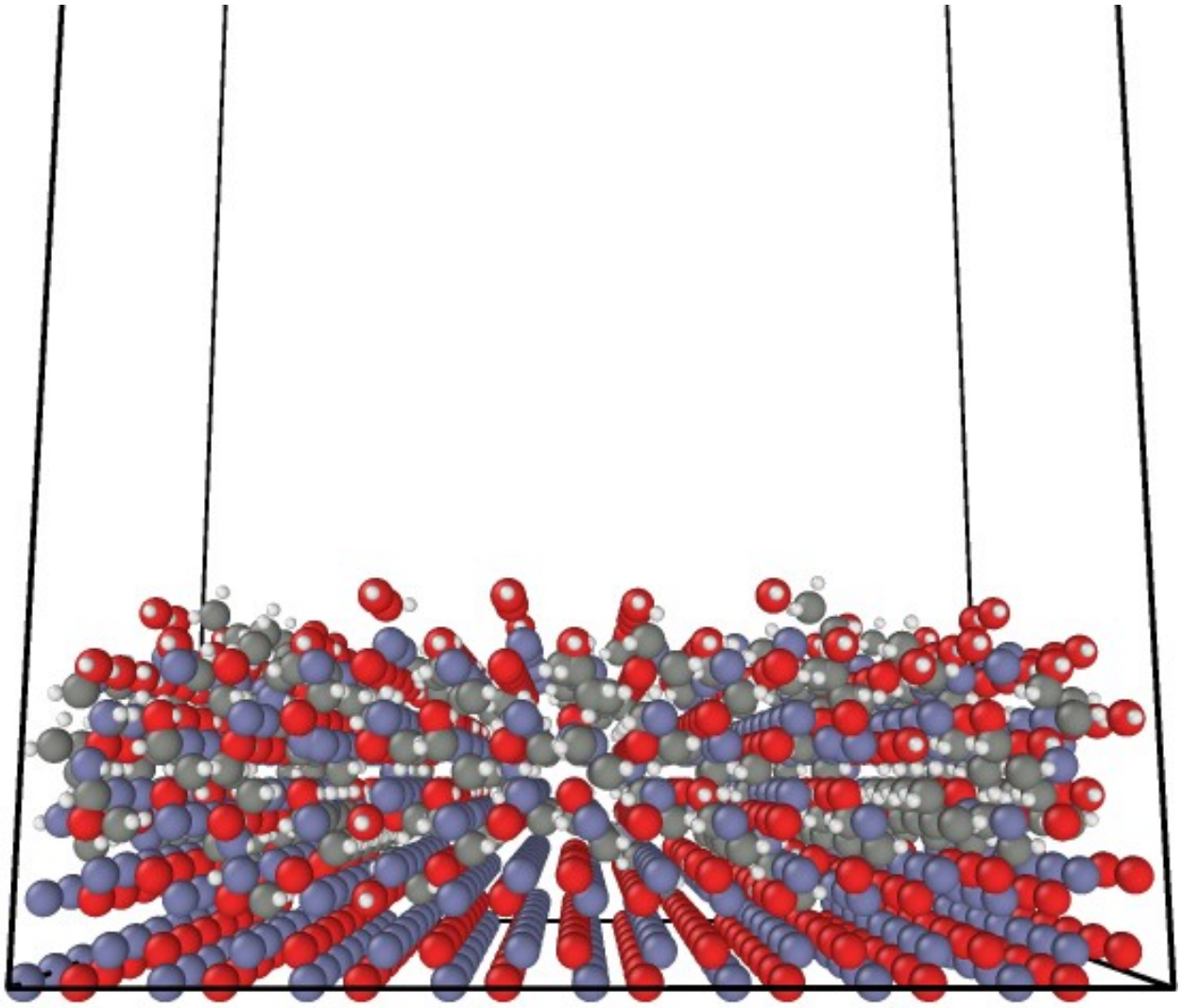

Figure 17. This image depicts the simulation box after eight ALD cycles. The zinc, oxygen, and hydrogen atoms represented in blue, red, and white respectively. Carbon atoms forming trapped ethyl ligands are shown in gray.

Future simulations will use this code as a starting point, changing only a few parameters at a time. Once the ZnO code is calibrated by comparing data from this default simuation to that reported by Weckman, the code and the researcher can be considered calibrated or zeroed out.

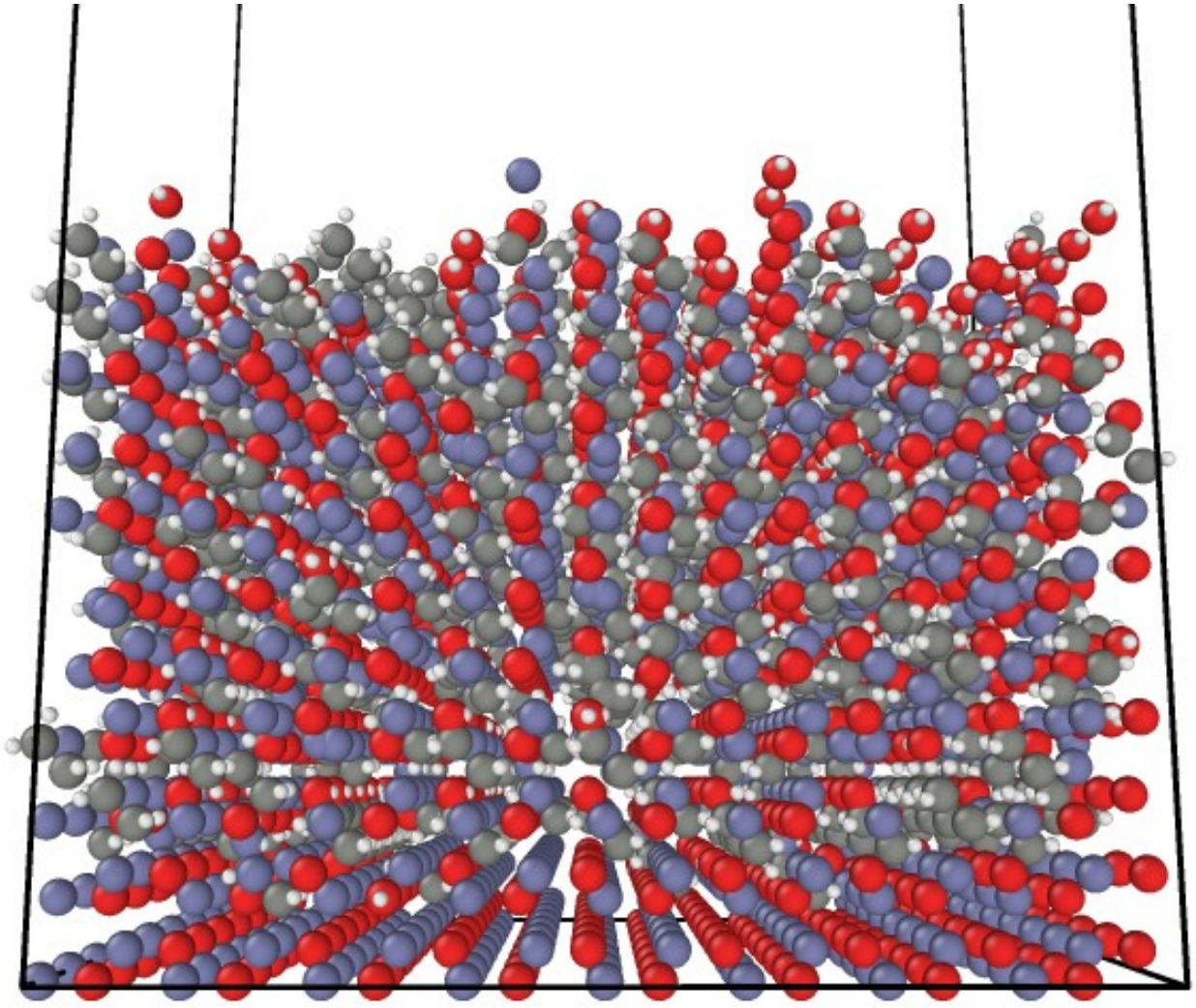

Figure 18. This image depicts the simulation box after 16 ALD cycles. The zinc, oxygen, and hydrogen atoms represented in blue, red, and white respectively. Carbon atoms forming trapped ethyl ligands are shown in gray.

3.1.1. Calibration of the ZnO Code. The calibration of the KMC code to match Weckman's results serves as the control for the ZnO simulations. Following Weckman's experimental methods,

the ZnO code was run for various temperatures including 300K, 350K, and 400K. These simulati ons of different temperatures were created by updating the reaction rates using and

the appropriate temperature parameter from Table 9 and Table 10. in the example input

script provided by Weckman. This example input script already defines the reactions possible and associated energy barriers. Also declared in the example script are the pulse and purge lengths of 0.7 seconds and 0.1 seconds respectively. Several simulations were run for each temperature using several different seeds for the SPPARKS random number generator. The data was then averaged amongst these simulations.

3.1.1.A. Mass vs Time. The mass of the simulated material increases in a stepwise function. As observed by Weckman and confirmed by experiment, the average mass gained during each deposition cycle is approximately 150 ng/cm^2 at temperatures of 400K and above [11]. This is well within accepted values in reference literature [3,4,17]. A comparison of the mass-time curves at different temperatures is made in Figure 19.

At the beginning of the water pulse there is an initial increase of mass followed by a near-negligible drop in mass as the water molecules remove the ethyl ligands. The increase in mass per cycle appears to remain uniform after the second cycle of deposition.

3.1.1.B. Standard Deviation of Mass vs Time. Due to the stochastic nature of KMC, four simulations were run for each temperature so that their data could be averaged. This poses the question of how much each simulation varies from its peers. The standard deviation of mass over time calculated at temperatures of 300K and 400K. The standard deviation in mass-time curves is plotted in Figure 20.

There is a spike in the standard deviations at the very beginning of every simulation in the amount of 54.3 ng. This spike was removed from the data. Generally, the standard deviation decreases with temperature. The maximum standard deviation in mass was 76.5 ng at 300K which is double the standard deviation of 30.7 ng at 400K. Standard deviation remains chaotic for the first half of the simulation then a direct relationship between time and standard

deviation appears. As time goes on, the standard deviation seems to increase. The slope of this curve at 400K is steeper than at 300K so simulations that run for longer periods of time may find that the standard deviation at high temperatures is higher than the lower temperature which appear to be plateauing towards the end of the 10-cycle simulation.

Overall, the maximum standard deviations are negligible at about 6.2% of the difference between the mass at 300K and 400K. This means that the standard deviation in mass is low enough to be able to justify the qualitative observations in these ZnO experiments. The standard deviation could be decreased with a larger pool of identical simulations run with various seed numbers for the SPPARKS random number generator.

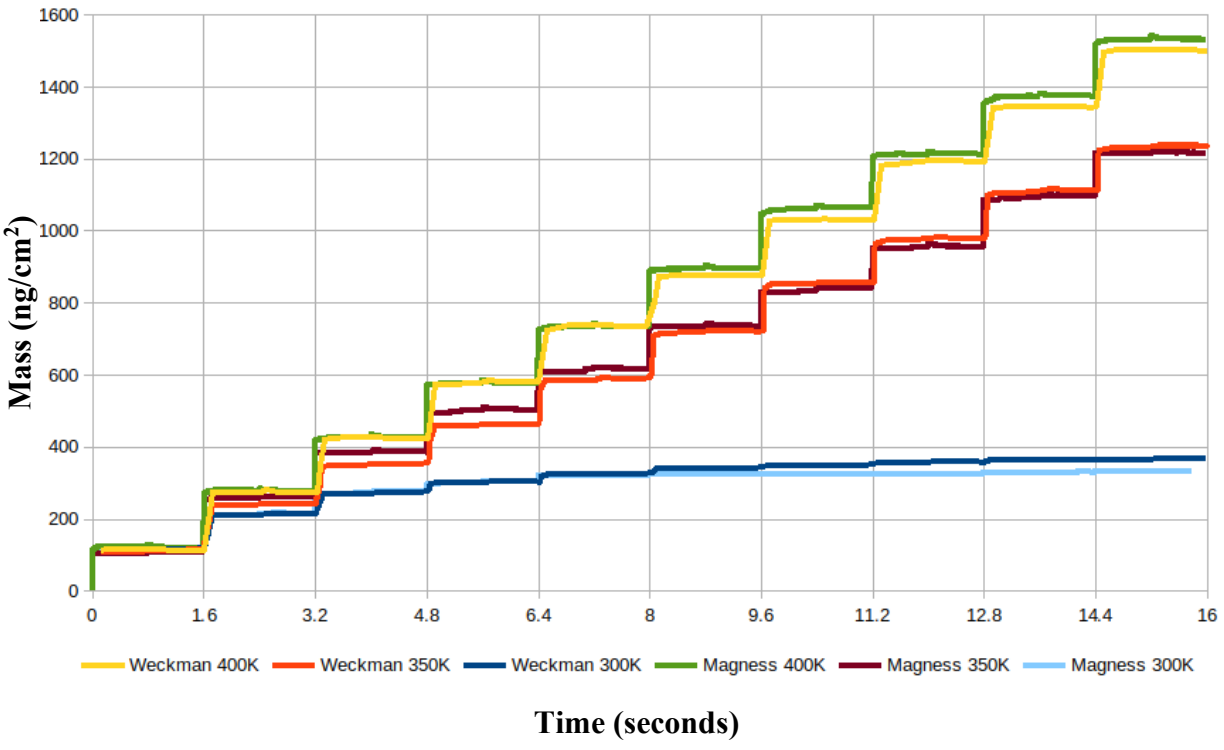

Figure 19. Plots of simulated mass-time curves for various temperatures are compared to results from Weckman's Thesis on simulated ZnO ALD.

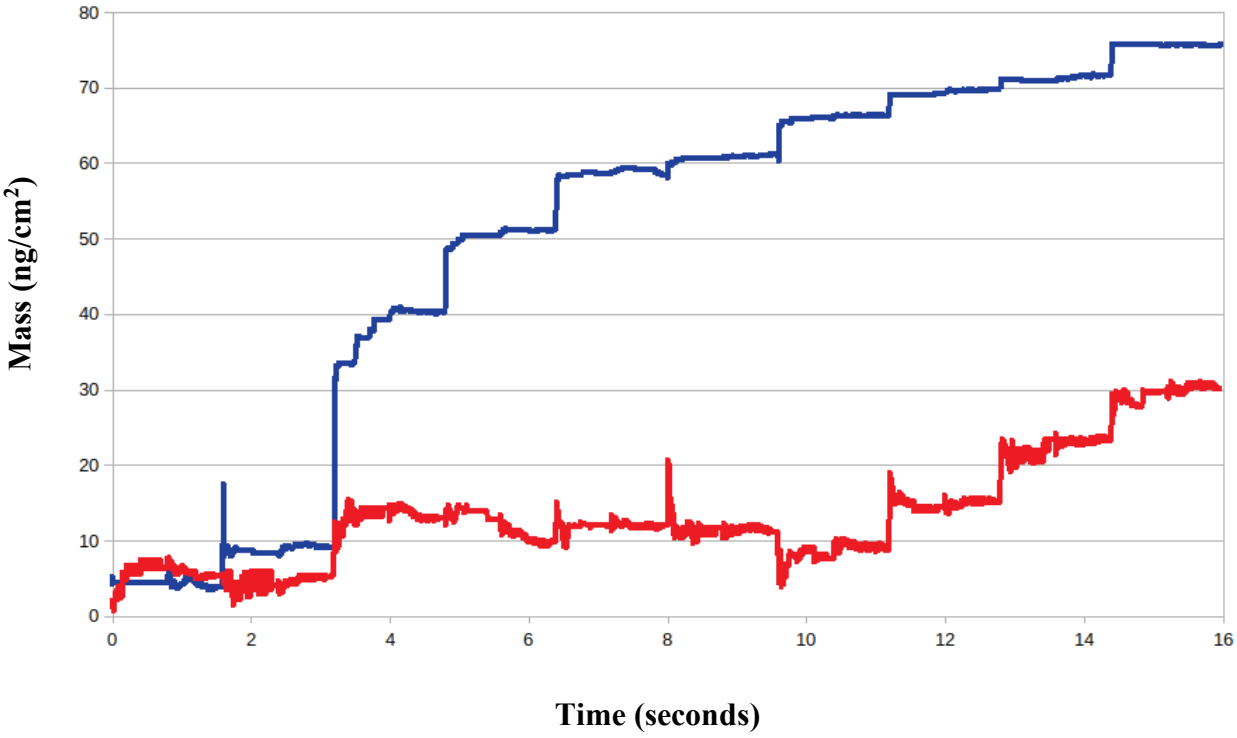

Figure 20. Plots of the standard deviation in simulated mass-time curves for simulations of the identical parameters. Standard deviation of high and low temperature simulation sets are shown in red and blue respectively.

3.1.1.C. Resultant Stoichiometry vs Temperature. The calibration procedure was rerun for pulse and purge times of 0.06 seconds in order to match experimental parameters to which these stochastic results will be compared. The metrics analyzed in this section include the atomic ratio of oxygen to Carbon, atomic percentage of hydrogen, and the atomic percentage of Carbon.

Average simulated O:Zn ratios range from 0.93 to 0.91 while experimental results obtained by X-Ray Photoelectric Spectroscopy (XPS) range from 1.09 toe 0.905 [4]. At higher temperatures the O:Zn ratio converges with experimental results. However, at 375 K the simulated ratios are lower than experimental results by 15.6% of the experimental value. The O:Zn versus temperature curves are plotted in Figure 21.

The simulated carbon content was also measured as an average atomic percentage. The simulated carbon content is generally lower than the experimental data from the literature. However, the relationship between simulated carbon content and temperature are quite similar in Figure 22.

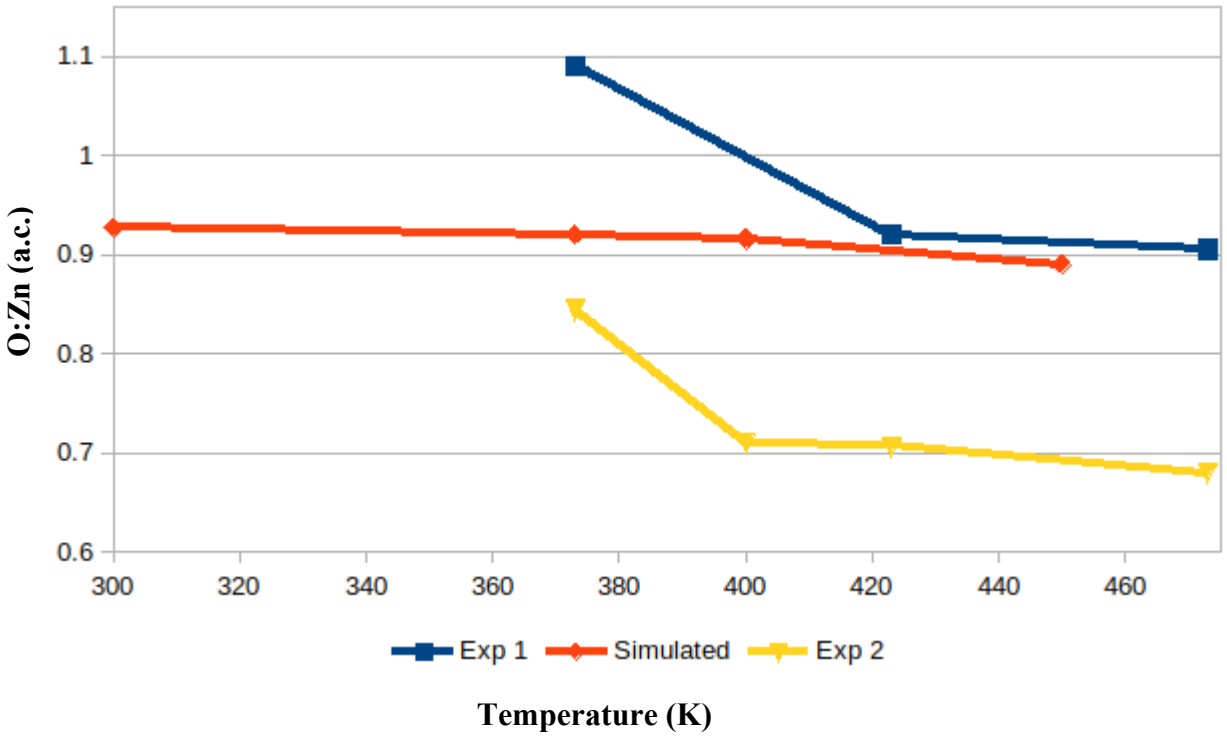

Figure 21. Plots of the atomic count ratio of oxygen to zinc vesus temperature are compared with two experiments from the literature.

The simulated hydrogen content was similarly measured and compared to experimental results from the same literature. While the simulated results present a more linear trend the experimental results clearly follow a decreasing natural exponential function. However, the general trend is negative and is quantitatively close to the experimental results as the difference between the two curves is at most 0.07 percent. It is hypothesized that another data point at 350 K would illuminate a pattern similar to that of the experimental data in the same plot. Thus, the

value would remain constant until approximately 350 K where the value begins to drop in dramatic fashion as ethyl ligands are now more easily removed at the higher temperature. This is supported by the plots in Figure 22 and Figure 23.

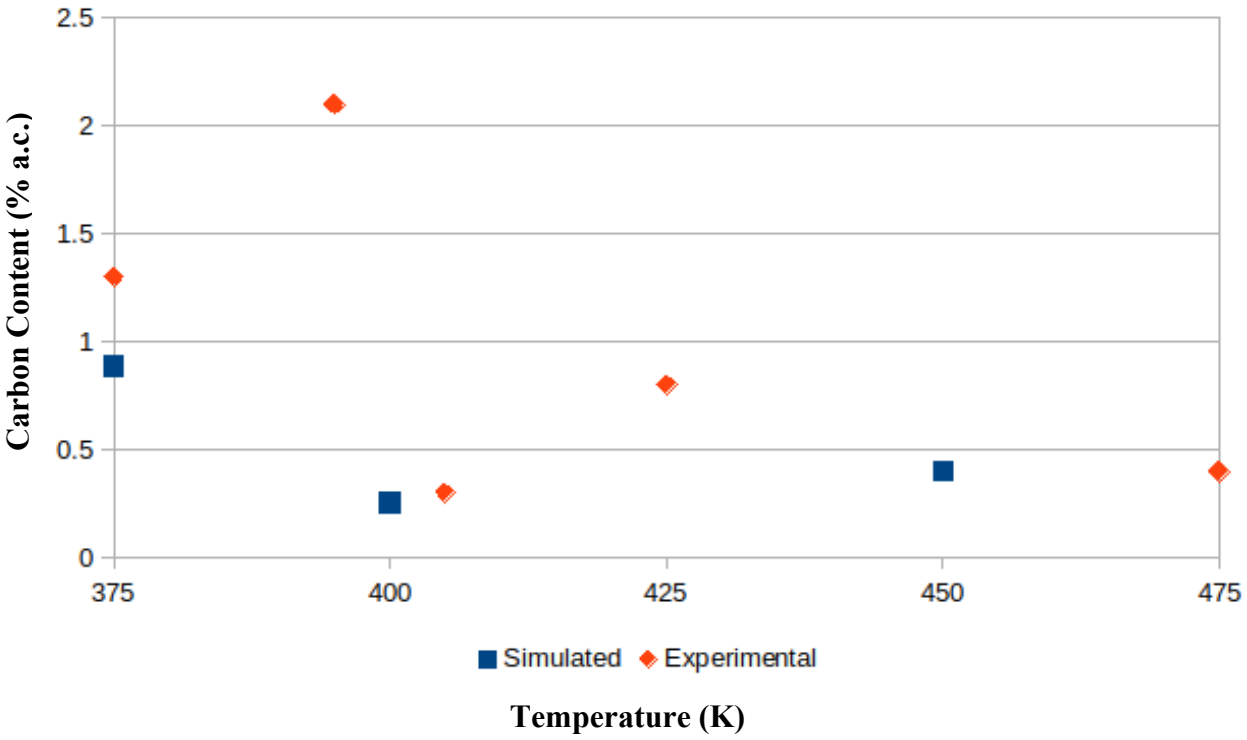

Figure 22. Plots of the atomic count percentage of carbon versus temperature are compared with two experiments from the literature.

Overall, the simulated stoichiometry qualitatively aligns with reference data. The hydrogen content decreases with temperature while the Carbon content has a more chaotic relationship with temperature. This reveals that hydroxyl and water molecules are more readily removed at higher temperatures while they tend to get trapped in the surface at lower temperatures. This is supported by the negative correlation between ethyl ligands and temperature as shown in plots of carbon and hydrogen content in Figure 22 and Figure 23.

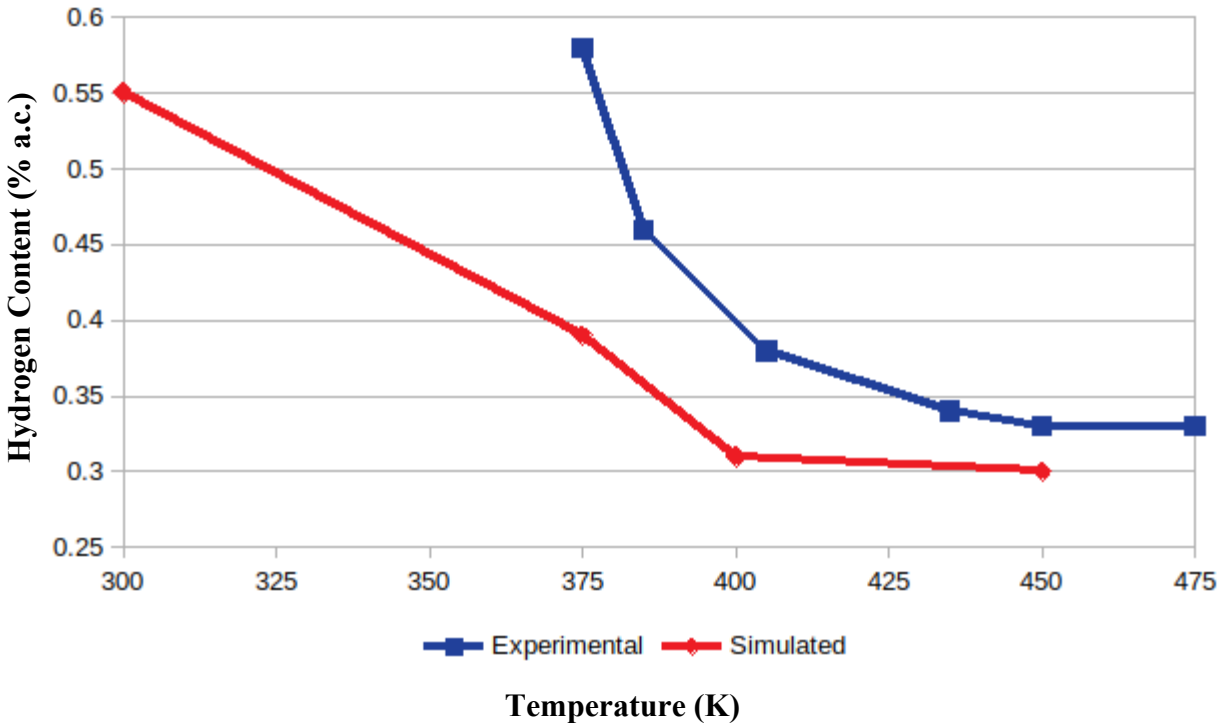

Figure 23. Plots of the atomic count percentage of hydrogen versus temperature are compared with experimental results from the literature.

3.1.2. Pressure Response Experiment. Again, using the example script as a stating template, the pressure was varied for several temperatures and pressures by adjusting the rate coefficients in the script. High pressure runs are set at 1 atm or 101325 Pa while the lowest pressure runs were performed at 2 Pa [17]. These simulations showed a positive correlation between pressure and mass gained per cycle in agreement with experiments from the literature.

3.1.3. Water Coverage Experiment. The impact of water coverage on the initial surface was tested. This aspect of study is relevant and critical in light of the recent advances in the ALD process for tunnel barrier synthesis that utilizes a wetting layer prior to the water pulse in the ALD process [1,2]. The overarching goal of adding a reactive metallic wetting layer is typically to maximize water coverage.

The default ZnO simulation serves as the 100% coverage case with all available oxygen sites containing a water molecule. Incrementally, the water molecules were removed from the initial surface and the simulation rerun. The deleted water molecules were selected randomly. The data was averaged over several seeds.

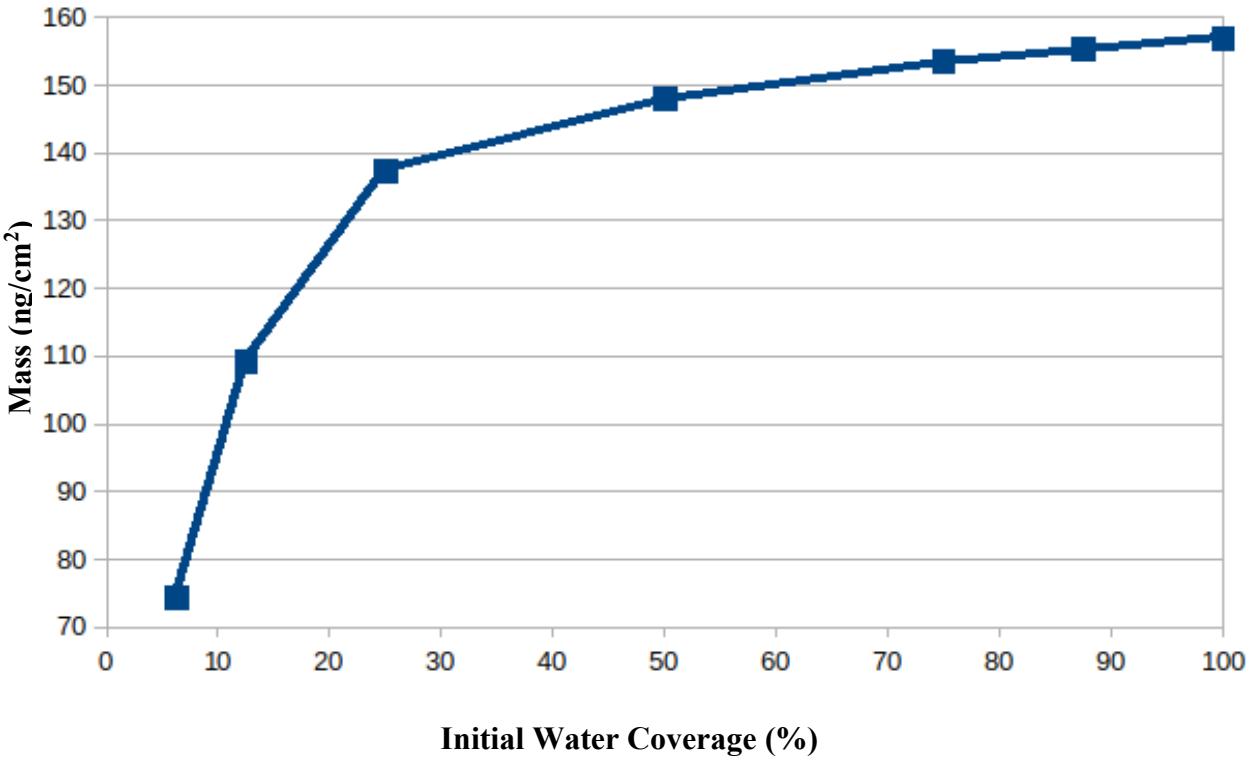

Figure 24. The average mass-gain per cycle is plotted against percentage of the initial surface that was covered with water.

3.1.3.A. Growth Per Cycle. GPC is not linear but directly correlates with water coverage. The maximum GPC of approximately 159 ng/cm^2 occurs at 100% water coverage of the initial surface. Meanwhile at 6.25% coverage the GPC is reduced to approximately 75 ng/cm^2, or about half of the maximum value. Figure 25 on the next page will show that the water coverage of the initial surface has a direct impact on the GPC of depositions of less than 16 cycles.

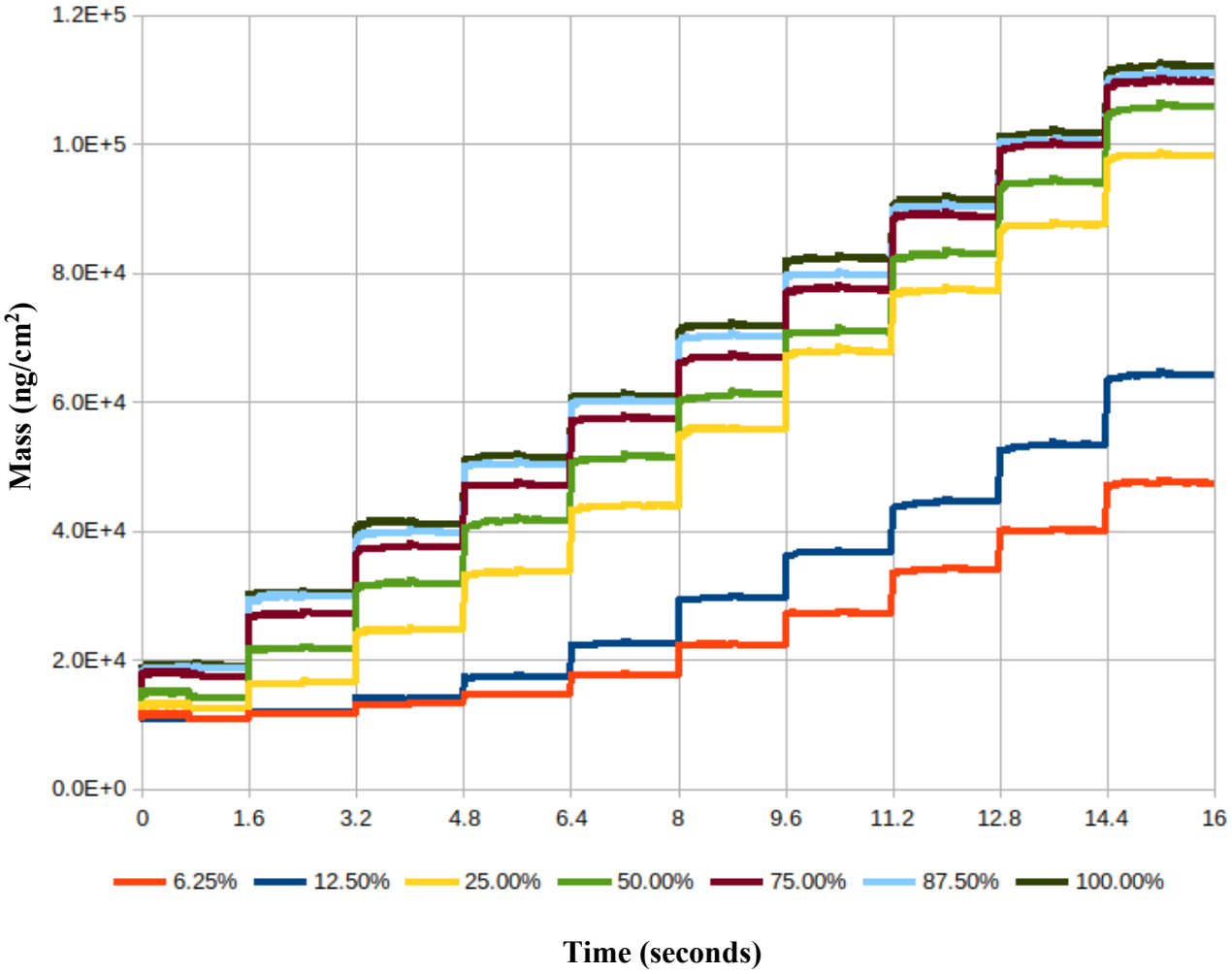

Figure 25. Plots of simulated mass-time curves for various percentages of water on the initial surface.

While the high coverage advantage in GPC is clear for a limited number of cycles, the mass-gain for low coverages increases linearly with time. The change in mass-gain is 12.72 ng/cm^2 per cycle. Thus, it is likely that the average GPC for the various initial coverages will converge after approximately 13 deposition cycles.

The data suggests that there is a minimum level of water coverage needed to ensure a higher quality of tunnel barrier. As shown in the Figure 24 and Figure 25, if the initial coverage exceeds 25% of the total area, a reasonably high mass gain can be obtained for at least up to

eight cycles of deposition. Beyond this level of coverage, the mass gain seems to be fairly similar irrespective of the initial water coverage. Thus, as the targeted tunnel barrier thickness gets thinner, e.g. sub-nanometer thickness – which is equivalent to about 4-6 cycles, the initial water coverage becomes critical [1,2].

3.1.3.B. Low-Coverage Growth and Clustering. In several low-coverage cases, specifically in initial coverages of 6.25% and 12.5%, there was no growth. These simulations terminated before the end of the first DEZ pulse. It was observed that this early terminating behavior occurred where the initial water molecules were distanced from each other. However, when clusters of water molecules existed in the initial surface, stable growth occurred. The reason for this behavior is that the event list becomes empty and the simulation prematurely jumps to the end of the simulation. These early terminating simulations were removed from the data and replaced with data from simulations with identical parameters except for the placement of the water molecules on the initial surface. The placement of the water molecules on the surface was again determined randomly.

The event list becomes empty because the hydrogen gets used up converting nearby DEZ to MEZ, thus no ligand-free sites are available to which more DEZ can adsorb. In addition, because of the distance between water molecules, proton diffusion becomes impossible. It follows that no interactions can take place as only MEZ and DEZ remain on the surface until the next water pulse. This leads to the terminal condition where the event list is empty and therefore the timestep jumps past the next pulse and to the end of the simulation.

As stated in the previous section, it is apparent from these observations that the amount of water coverage on the initial surface is relevant for depositions of only a few cycles, but not as much for depositions consisting of many cycles. Clusters of water molecules are required for any

meaningful growth, especially for ultrathin tunnel barriers. These ultrathin devices are made with a limited number of deposition cycles highlighting the emphasis of short term dempositions such as the 16 cycle simulations used in many of the targeted studies presented later within this document.

It is unclear whether the effect of water clusters on the initial surface matches experimental values or results until there is a practical resolution to the terminal condition feature of the KMC code. For similar reasons the investigations of initial surfaces consisting exclusively of O can't be performed unless the water pulse is reversed as done in the previous simulation set.

3.1.3.C. Effects of Initial Water Coverage on Stoichiometry. Again, we look at the stoichiometry of the simulated material. In Figure 26 the O:Zn ratio is plotted against the initial percentage of water coverage on the starting surface. The ratio is calculated two different ways. The lower line represents the ratio of number of sites in the lattice that contain oxygen versus the number of sites that contain zinc. The upper line represents the ratio only factoring in the pure oxygen and pure zinc sites. This means that the number of pure oxygen sites tends to be greater than the number of pure zinc sites in the lattice. However, the number of oxygen-containing sites tends to be less than the number of zinc-containing sites. This means that there are more impurities due to the ligands attached to zinc atoms than there are due to the number of trapped water and hydroxyl molecules combined. Both of these lines straddle the ideal value for ZnO of unity. The pure ratio matches closely with the default simulated value at 100% coverage. Both ratios start relatively close to unity and begin to diverge as the initial water coverage increases.

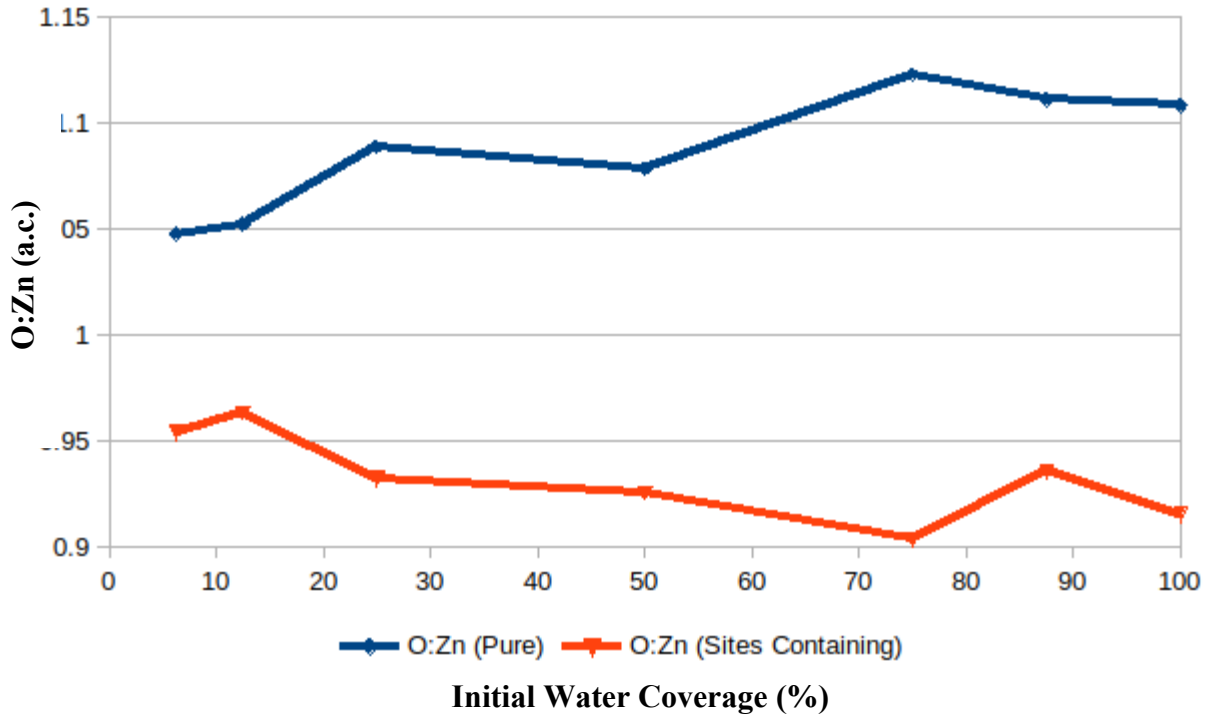

Figure 26. The ratio of oxygen to zinc atoms are compared with the ratio of oxygen-containing sites to zinc-containing sites.

3.1.4. Other Initial Surfaces. Other initial surfaces were tested to see their effects on ZnO growth. The default simulation script for ZnO was used and only the initial surface was varied. In this section, different initial surfaces are created by replacing the water molecules in the default ZnO simulation with various other species. The initial slab is tested with oxygen sites on the surface, with hydroxyl molecules on the surface, and with zinc sites on the surface. Some, if not most, of these simulations require the DEZ and H2O pulses to be reversed with the water pulse coming first. The mass-time curve for this simulation can be seen in Figure 27.

3.1.4.A. Oxygen Covered ZnO. First, the water molecules were replaced by O molecules. Now the initial surface takes the form of a ZnO slab with oxygen exposed on top. This simulation failed. There reason for simulation failure is because there is no hydrogen on the surface. The absence of hydrogen limits the number of events in the reaction list, specifically

prohibiting the adsorption of DEZ. This leads to the previously mentioned terminal condition where the KMC code skips to the simulation end.

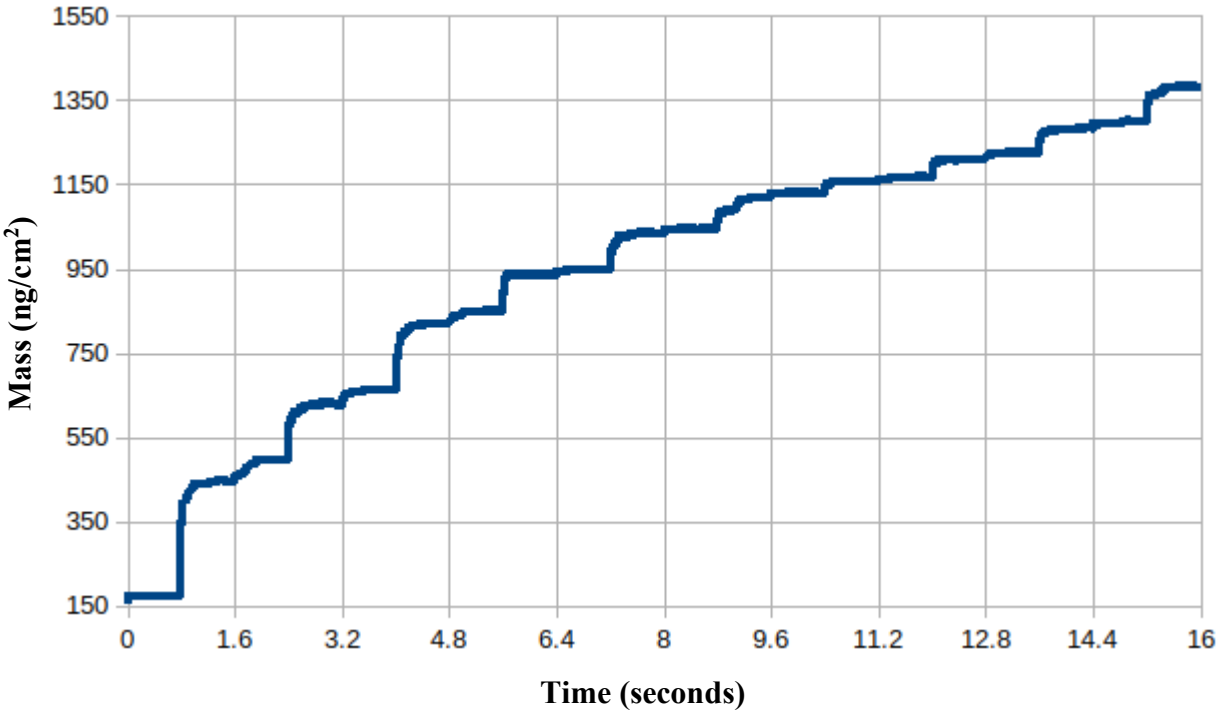

Figure 27. Mass-gain curve of simulation with an initial surface covered with oxygen; pulse sequence was reversed so that the water pulse occurred first.

However, by reversing the pulses the simulation was able to play out. This is because during the now initial water pulse, the water adsorbed onto available zinc sites allowing proton diffusion to occur. The average mass-gain per cycle under this regime is approximately 120 ng/cm^2 which is less than the default simulation. The reason for the lower mass-gain value is because the first half-cycle is a water pulse which does not increase the mass as much as a DEZ pulse would. Stoichiometry versus time for this simulation can be analyzed in Figure 28 and Figure 29. The figures look at the ratio of oxygen to zinc and the amount of hydrogen in the system respectively.

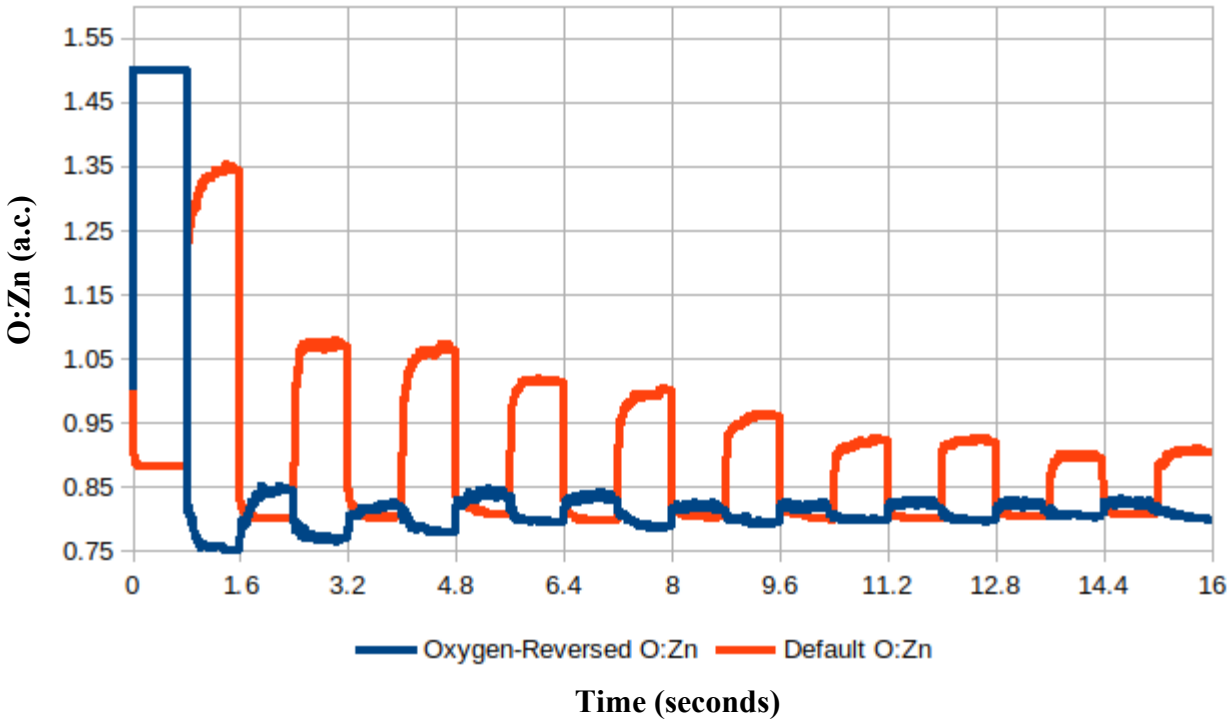

Figure 28. The ratio of oxygen to zinc atoms are compared between the default simulation and the simulation when a water pulse occurred first.

Further comparing the mass-gain to the mass-gain of the default ZnO simulation it can be seen that this initial surface does how the mass changes with each cycle. Notice that the DEZ pulse does not saturate the surface as quickly as default simulation. By comparing the O:Zn of this regime to that of the default Zno simulation it can be seen that this ratio closely matches the default during the DEZ pulses with a difference of 4 percent. According to this there is relatively higher amount of oxygen in the default simulation during the water pulse than there is in the default ZnO simulation. By looking at the relative hydrogen counts between the two types of simulations, a difference in hydrogen content can also be observed in Figure 23. More hydrogen is removed during the first DEZ pulse in the default ZnO simulation than under this regime. Hydrogen content increases during the water pulse and this makes sense as the water pulse is the source of the oxygen and hydrogen for these types of deposition.

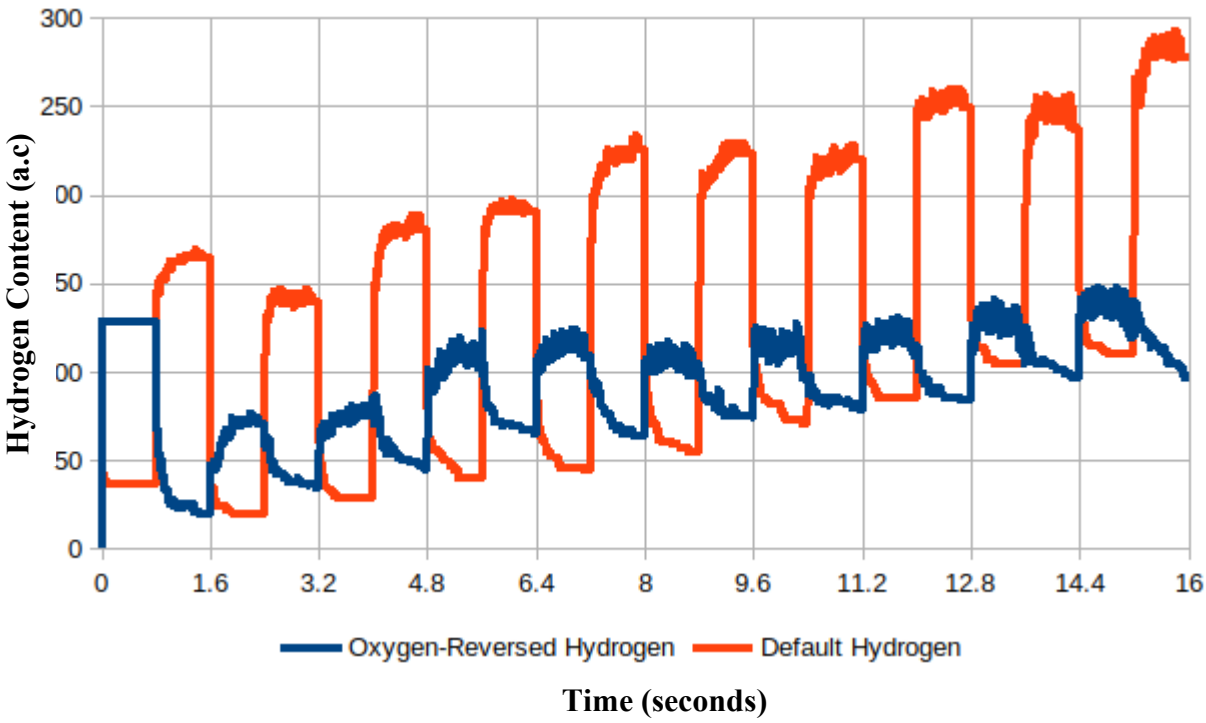

Figure 29. The ratio of amount of hydrogen in the default simulation are compared to the simulation where the water pulse occurred first.

These observations suggest that during the initial water pulse, the incoming water will adsorb to the surface and diffuse its protons to the bare oxygen sites on the surface. The incoming water then becomes OH or more bare oxygen sites with little water remaining. The OH and bare oxygen sites do not react with DEZ as readily as water. In fact, when performing this experiment again with an OH surface, the simulation stops due to the previously mentioned terminal condition where the simulation clock jumps to the end of the simulation. This stunted growth during the first cycle negatively affects later deposition cycles.

3.1.4.B. Zinc-Covered ZnO. In this experiment, the water molecules on the initial surface from the default ZnO simulation were replaced with zinc atoms. As such, the initial surface again is a layer of ZnO with zinc sprinkled on top. Starting with the initial DEZ pulse causes the simulation to fail as there is no reaction defined for DEZ to adsorb to zinc sites. Therefore, the

pulses were again reversed from the default ZnO simulation settings and water was pulsed first. This is another way to simulate a flood of water prior to the beginning of deposition.

The water adsorbs to the zinc sites but unlike the previous experiment with the oxygen-coated initial surface, this zinc-coated initial surface regime does not accept protons from the incoming water. Therefore, proton diffusion does not occur and water molecules remain intact on the surface at the end of this initial water pulse. Thus, the initial surface at the end of this first water pulse is similar to that of the initial surface of the default ZnO simulation. Despite less than stellar mass—gain during this initial water pulse, the remainder of the pulses act similarly to the default surface. Again, the mass-gain is reduced from that of the default ZnO simulation but the difference in mass is due to there being one less DEZ pulse than the default ZnO simulation.

3.1.5. Fast Breakdown of DEZ. DEZ was not observed during the default ZnO simulation. However, there is no other way for ligands to appear in the lattice without the prior adsorption of DEZ. Thus, the reaction must be occurring without being listed in any log or dump file. The explanation is purely computational: The breakdown of DEZ occurs at timesteps smaller than the time between log entries. To be clear, the simulation is updated in variable timesteps described by Equation 2. However, the log file is updated every 0.001 seconds and the dump file is updated every 0.005 seconds by default.

To investigate how quickly the DEZ breakdown reactions occur, the log file timesteps were set to increasingly shorter intervals. DEZ site species were visible at timesteps on the order of a microsecond, after which time they decompose into an MEZ site species. At the simulation start, this behavior manifests as the adsorption of a DEZ onto a water molecule, an ethyl ligand and hydrogen atom are removed from the DEZ and water respectively, leaving an MEZ on-top of a hydroxyl group leftover. This MEZ then jumps onto a neighboring site in the zinc sub-

lattice some point during the next time step. The MEZ will persist on the surface until a following water pulse removes the ethyl ligand. In the event that the MEZ is not removed by a subsequent water pulse, it will become trapped in the surface.

3.1.6. H2O Pulse First. Replicating the default experiment with the pulses reversed was done by exposing the surface to water first, the surface gains hydrogen and proceeds in a manner similar to the default simulation after the first DEZ pulse begins. The average mass-gain per cycle is 135 ng/cm^2 which is less than the value for the default simulation. The reason for this discrepancy is that the mass-gain during the initial water pulse was negligible. The incoming water only donated hydrogens onto the surface which have negligible mass compared to the mass-gain during the DEZ pulse.

3.2. Al_2O_3 Simulations

Each of the Al_2O_3 simulations were conducted on a lattice consisting of 5760 sites. This lattice is based on a supercell of α-Al_2O_3 with the following parameters for the supercell listed in Table 16 below. The temperature of this default Al_2O_3 simulation is again 400K with a pressure of 20 Pa. The default pulse and purge times have been set at 0.05 seconds each to closely match experimental parameters to which we compare these results. In this series of simulations of Al_2O_3 ALD, the effects of temperature, pressure, and OH coverage on the initial surface on deposition are explored.

Table 16. Dimensions of Al_2O_3 Simulation Box

	A (Angstroms)	B (Angstroms)	C (Angstroms)
Super Cell	24.025	38.44	52.47

3.2.1. Al_2O_3 Control. Just as previously done with ZnO ALD, this experiment tests the effect of temperature of Al_2O_3 deposition. The default simulation was adapted by updating the reaction rates and temperature parameters with the appropriate values from Table 5, Table 7, and Table 11. This was done for a set of simulations at 375 K. This data is compared to experimental results from the literature.

3.2.1.A. Mass Gain. Mass-gain data for several simulations at 375 K were averaged and the results were normalized to the maximum mass during the cycle. The time dimension was normalized to the length of a single pulse. The ratio of mass gained during the DEZ pulse to the mass gained during the water pulse closely corresponds between simulation and experiment. The simulated mass gained during the DEZ pulse was 80 percent of the maximum mass while the experimental value was 67 percent as seen in Figure 30.

However, a quantitative analysis shows that while the experimental mass gained per cycle is about 35 ng/cm^2 while the simulated value is 750 ng/cm^2. This is much higher than the experimental values [6,18,19,20]. The discrepancy in mass gained can be attributed to the lack of steric hinderence in this model. Without repulsive forces between surface ligands and adsorbent ligands the mass is deposited at an exceptional rate unseen in physical deposition.

Additionally, it appears that up two layers of TMA can adsorb to the surface again, this is due to the mechanics of the code and specifically its lack of steric hinderence. This multilayer deposition during a single pulse accounts for the fact that the simulated mass increase is twice that of the mass of a fully saturated surface. To clarify, the change in mass is the mass of a single plane of sites but we see that the change in mass is roughly twice that of the mass of a single plane. There are 280 aluminum sites and 160 oxygen sites in a layer of the is hexagonally

packed Al_2O_3 lattice.

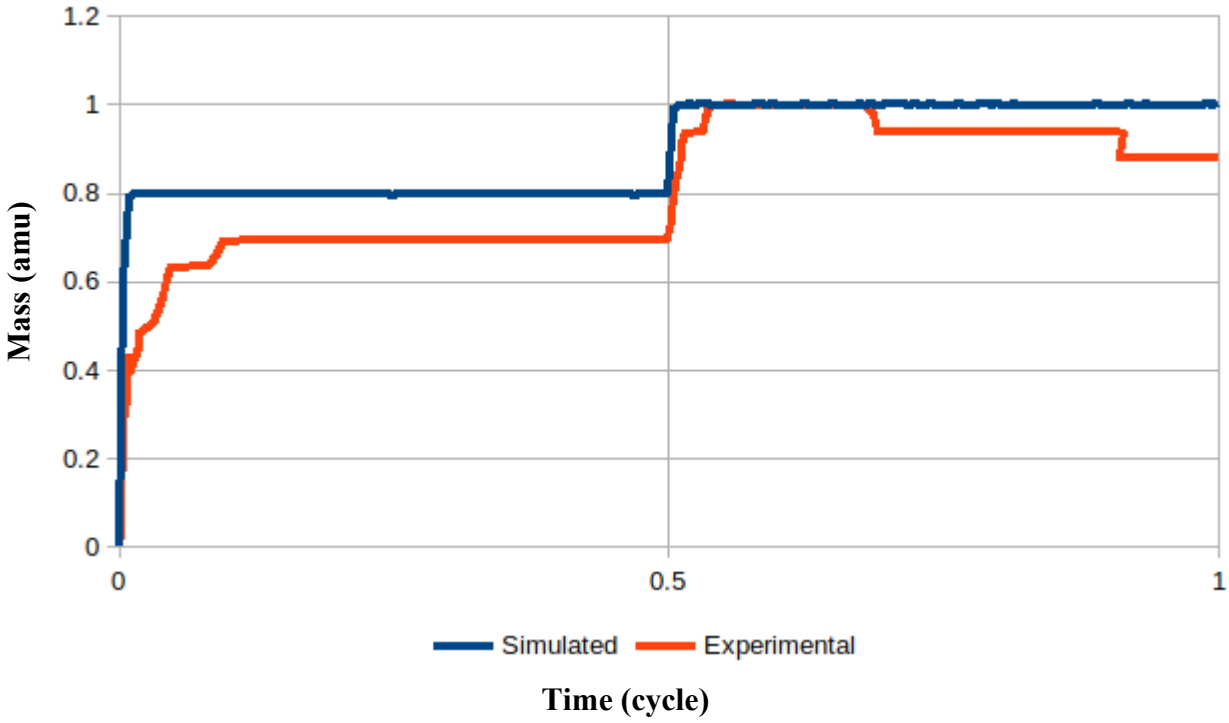

Figure 30. The mass-gain curves for simulation and experiment were normalized to the maximum change in mass during the cycle and the results are comparable.

With a relationship between experiment and a control simulation established we can now examine the effects of various parameters on mass-gain and qualitatively, if not quantitatively, compare it to the baseline control presented in experimental literature. Mass-time curves for different temperatures can be seen in Figure 31.

While the literature reports that Al_2O_3 deposition is possible at temperatures as low as 300 K all simulations below 335 K proceeded into the terminal condition state. It appears that below this temperature none of the chemical reactions included in the model can occur. More energy is needed for reactions that are possible with a ligand saturated surface. Average growth per cycle above 340 K remained relatively constant with temperature. Simulations up to 375 K

were conducted until the terminal condition began to strike again. Above this temperature reactions occur so quickly that the TMA pulse must be shortened in order to propagate the simulation and even then simulations with shorter TMA pulses did not produce more than one or two cycles and so this data was not included.

Thus, a direct relationship between temperature and average mass gain has been established with these simulations and qualitatively matches the experimental artifact where mass increases with temperature. However, this simulation presents a narrow window in temperature for ALD growth. Again, this is likely due to reactions that have not yet been included in this model.

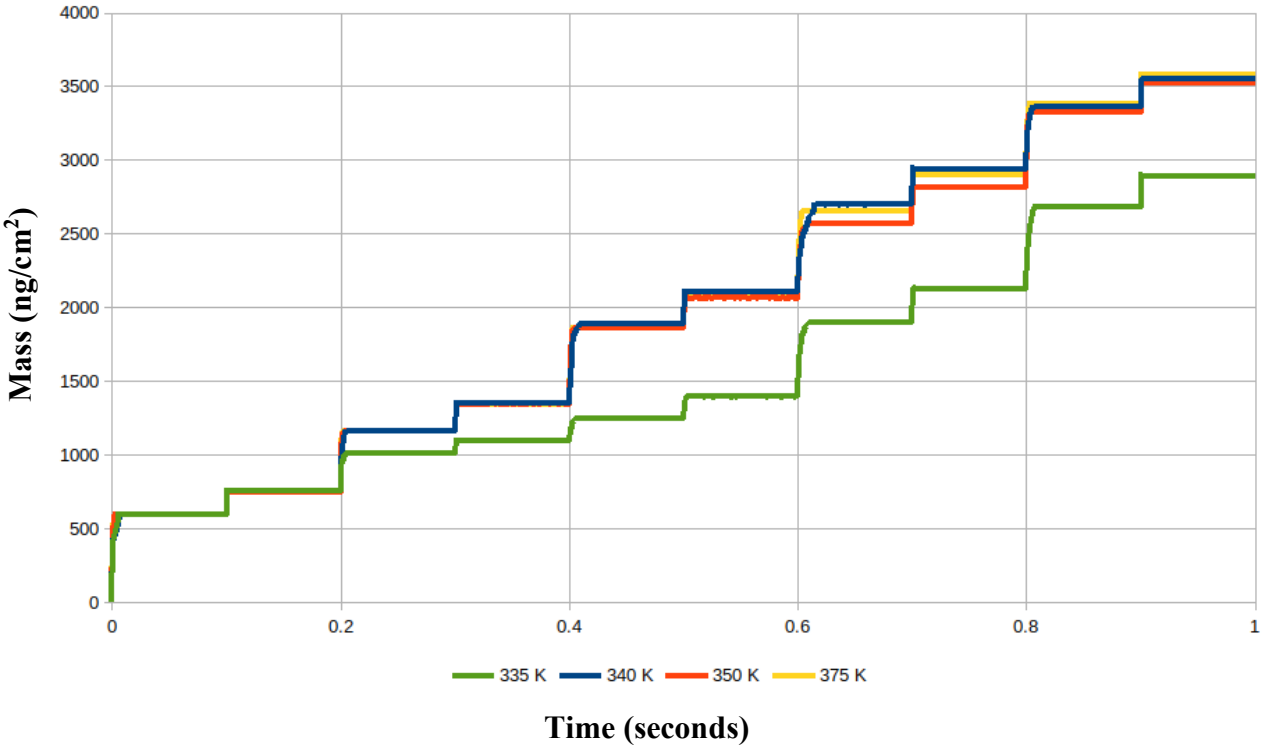

Figure 31. The mass-gain curves for the alumina deposition are plotted for various temperatures.

3.2.1.B. Stoichiometry. The code can produce a population count of each species within the lattice. Here the ratio of oxygen to aluminum is probed. The O:Al ratio fluxuates as deposition progresses through time and pulse-purge half-cycles, rising on the water pulses and dropping on the TMA pulses which makes sense. As deposition continues the O:Al ratio tends to increase slightly. It is likely that this increase will stop as deposition continues and a stable stoichiometry is achieved.

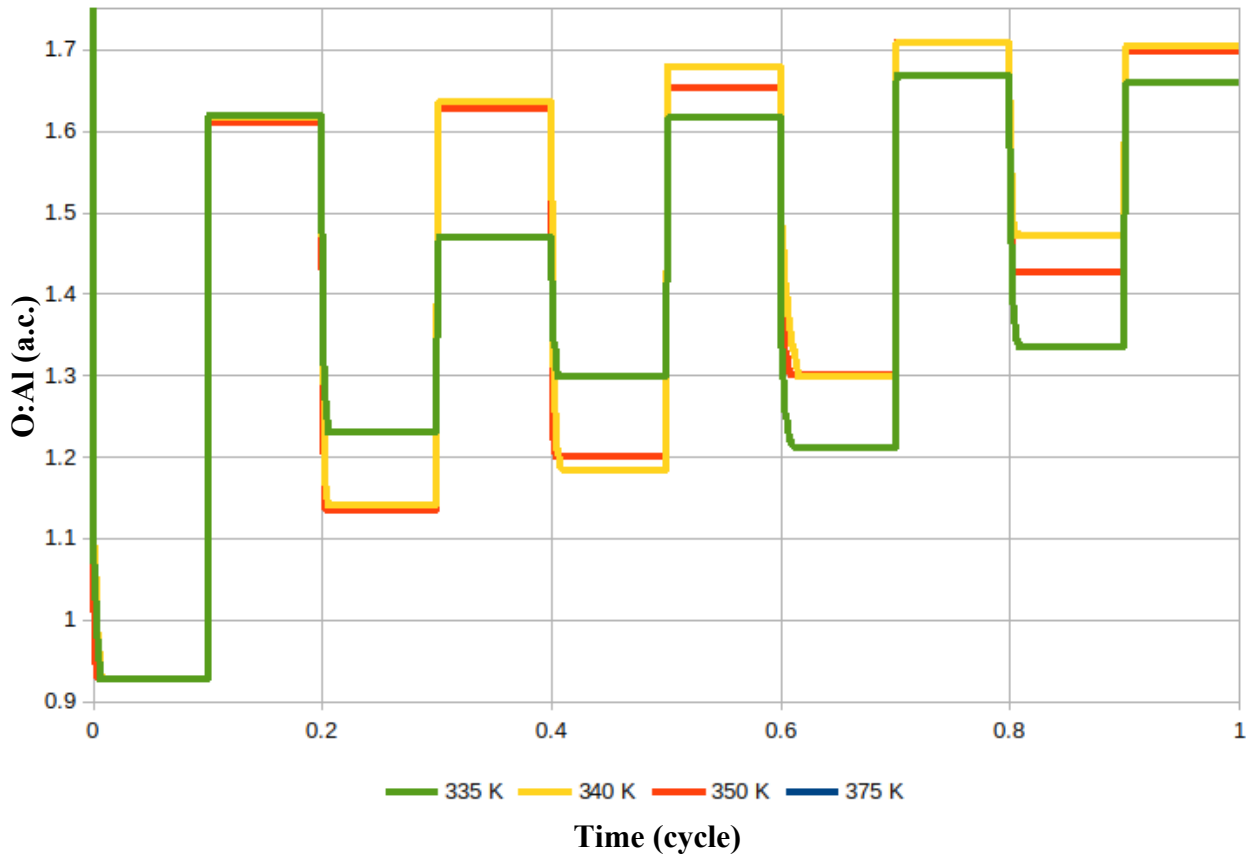

Figure 32. The ratio of oxygen to aluminum sites are plotted against time for various deposition temperatures.

Temperature seems to affect the O:Al ratio as follows. The high temperature runs, at 340 K and above, all closely match with each other. The simulation set at 335 K however reveals a different behavior. For the first cycle, the ratio is identical for all temperatures. During the

second deposition cycle the contrast in this ratio between the TMA pulse and the water pulse is much less than this same contrast for the higher temperature runs. In other words, the change in O:Al is 20.5 % for temperatures of 335 K while temperatures above this exhibit a change of 43.0 % during the second cycle. After this cycle the change in O:Al appears to converge with the high temperature runs albeit at a slightly lower value. At the end of five deposition cycles the ratio for 335 K is 1.66 and 1.70 for higher temperatures. This O:Al ratio is plotted versus time in Figure 32 for various temperatures.

3.2.2. Effects of Initial OH Coverage. In the same manner that the effects of water coverage on the initial surface was tested, the effects of initial OH coverage was also probed for the alumina deposition method. Again, a positive correlation was observed between OH coverage and mass-gain.

3.2.3. Fast Breakdown of TMA. In a similar manner to the regime where the fast reactions of DEZ were observed by decreasing the time between entries in the simulation log. As with the default ZnO simulations, the metal adsorbant precursor does not appear in visualizations of the simulation because it decomposes to quickly, on the same order of magnitude as for DEZ. This makes sense as the rate coefficients for these adsorbent precursors also happens to be on the same order of magnitude.

3.2.4. Pressure Response. In this sub-study, the effects of precursor pressure are studied and compared to experimental results from the literature. The experiment referenced here was done at 373 K for pressures of 760 Torr and 2 Torr which corresponds to 101,325 Pa and 266 Pa respectively [17,30]. The high-pressure run is also valued at 1 atmosphere. These parameters were used in the following simulations to test pressure response.

While the reference experiment used pulse and purge times of dozens of seconds, the default pulse and purge times of 0.05 seconds were used here [11]. The reasons for the use of shorter pulse purge times are that the simulation experiences the terminal condition at TMA pulse lengths greater than this and because longer pulse lengths would not affect the results.

The mass-gain is not affected by pulse length because most of the adsorption reactions occur at the beginning of each pulse. The terminal condition experienced due to longer TMA pulse times can be attributed to the lack of steric effects incorporated into this version of the KMC code. Without steric hinderance, the TMA adsorbs rapidly to the surface and all the reactions occur within 0.05 seconds. After this period no reactions are available because the surface becomes infested with TMA that decomposes to DMA. Without available chemical reactions in the event list the simulation jumps past the next cycle and to the end of the simulation. Thus, the use of shorter pulse times is reasonable justified.

When a chamber pressure of 1 atm was employed in the simulation, the simulation again experienced the terminal condition. Higher pressures yield a higher rate coefficient for the adsorption reactions and thus chokes out reactions by slamming the surface with the maximum amount of adsorbed particles. After a slew of simulated depositions at different pressures, the only one that were able to run were at pressures of 2 Pa and below. The Al_2O_3 default simulation temperature of 375 K was used here.

At high pressures experimental literature found that the mass-gain increases at a greater rate than the low-pressure experiment [21]. Figure 33 below is beautiful for several reasons. First, this graph demonstrates a direct correlation between mass gain and pressure in qualitative agreement with the literature. Second, this graph demonstrates that the code is capable of simulating more than five deposition cycles when the mass-gain is lower. Finally, and

most importantly, this experiment shows that the Al_2O_3 code produces mass gains that are congruent to higher pressure simulations.

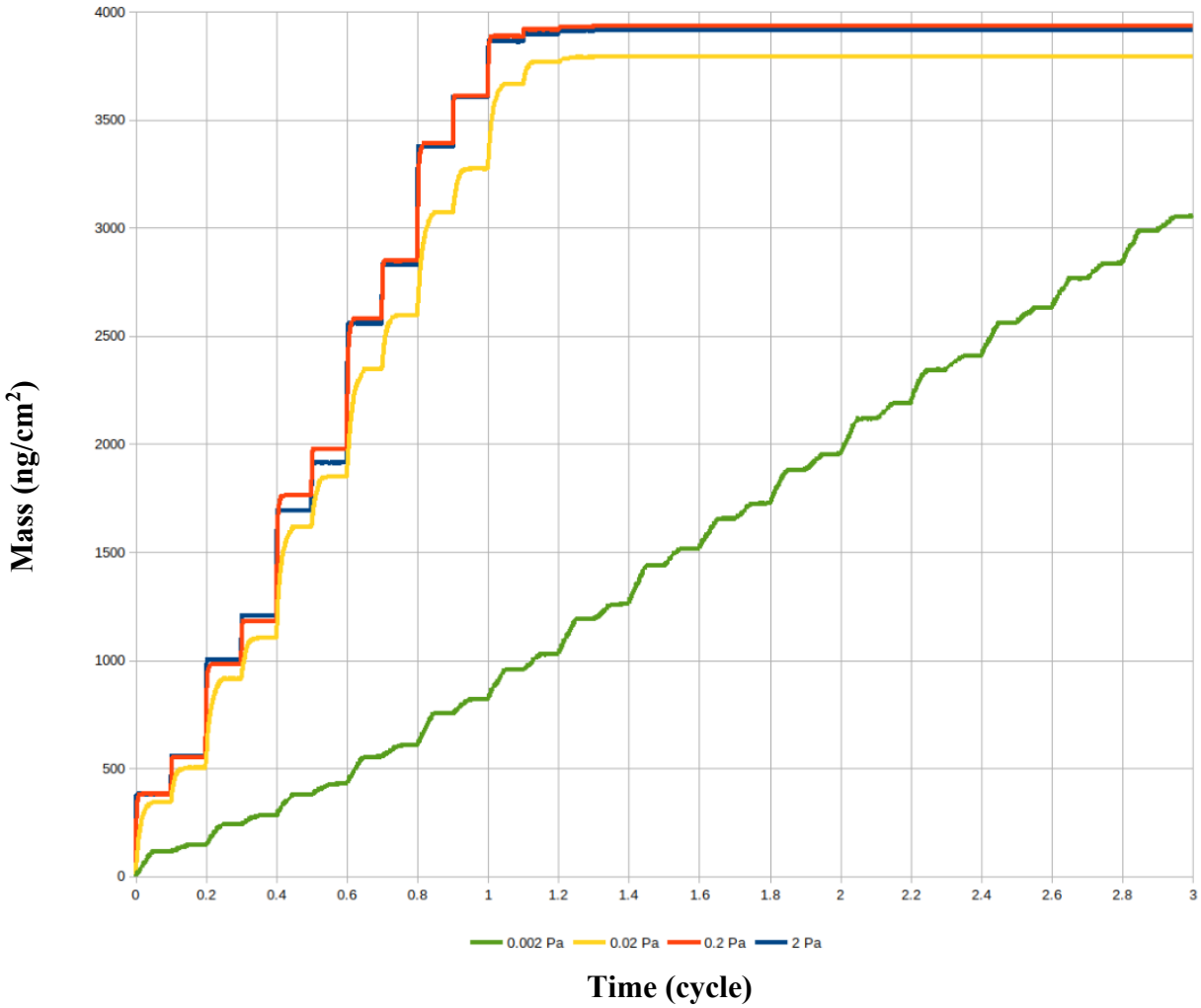

Figure 33. The mass-gain curves for the alumina deposition are plotted for various pressures.

This last observation is important because it appears that though shape of mass growth is not changed by pressure even though the actual values are changed. At last, there is some justification for the results found so far. Even though the simulated mass-gains have been calculated to be much greater than reported in experimental literature, they general behavior is the same. The meaningful takeaway point is that the lack of steric effects incorporated into the

model does not seem to affect the relative number chemical reactions only the overall population. Thus, the simulated results might be able to replicate experimental values by artificially reducing the pressure as a stand in for steric hinderence by limiting the number of adsorbed particles. Ultimately, this observation adorns this code with a bit more credibility. It is truly exciting to see such results even an incomplete reaction list with steric hinderance excluded.

4. DISCUSSION

Much work has been done to further the goal of ALD research via the KMC method and it is important to take minute to review the progress made here and set out some possible paths for future research in this area.

Information gleaned from this work reveals that KMC can indeed reveal relationships between deposition parameters and properties of the resultant material.

Several avenues of future work in this area of interest are outlined including possible ways to improve the KMC code, expanding the KMC code to simulate various situations, and the hybrid use of KMC and Machine Learning (ML) as a new way of simulating ALD.

4.1. Reflections

This study has confirmed the results produced by Timo Weckman with his ZnO KMC model [11]. With experiments investigating chamber pressure, the percent water coverage on the initial wetting layer, and testing of various initial surfaces this study has expanded upon the previous work. In addition to the expansion of the ZnO research a modified version of the KMC code was created to study the deposition of Al_2O_3 using reactions and energy barriers from Weckman's research. This code allows the study of mass, stoichiometry and more by varying parameters such as temperature, pressure, pulse time, and state of the initial surface.

4.1.1. Lessons from ZnO. The ZnO code proved an invaluable tool both as a means to investigate ZnO deposition but also to investigate the KMC method itself. Calibrating the code by independently matching Weckman's work was not just about the code; The researcher was being calibrated to the KMC method as well. Using KMC to model complex chemical reactions

is a forest one can easily get lost in. Comparing results to that of the previous code ensured that the experimental setups in this thesis were valid.

This work demonstrates for the first time that the KMC code can qualitatively simulate the material response to chamber pressure during deposition. Also examined was the effects of the starting surface. Here the code predicts that initial water coverage will affect the growth for only a few cycles but then behaves similarly regardless of the initial water coverage. This means that for thin materials of only a few nanometers in thickness this coverage parameter may be an important consideration.

The effects of a zinc coated initial surface was similar to starting with a water pulse on the default water covered surface. In both of these examples, the mass gain was similar to that of the default ZnO simulation with the exception that the initial pulse showed little to no gain in mass, essentially shifting the mass curve to the right by one half-cycle. Again, these initial surface parameters seem to affect depositions with only a few number of cycles.

4.1.2. Experiences from Al_2O_3. The insight gathered was not just simulated data being compared to experiment. While this KMC method is amazing in the fact that it allows us to simulate a physical process on the engineering time scale, the downside is that much work must be done beforehand. Event lists must be created with appropriate rate coefficients as well as energy barriers that can each take days to calculate. A lattice must be setup and worst of all is that six separate files in SPPARKS source code of the KMC model must be created or modified in order for this method to work [13].

But the beauty of adopting KMC becomes apparent when looking at the results from the Al_2O_3 model. While the data the model produces does not quantitatively match experimental results, it fundamentally demonstrates similar responses to the adjustable parameters in

ways similar to physical deposition experiments. The normalized mass-gain is an example of how well the code works. It was able to simulate the behavior of the mass taken from experimental literature. While the average mass gained per cycle did not quantitatively match experiment, the simulated ratio of mass gained during the TMA pulse versus the water pulse did match with experimental data from the literature.

4.2. Paths Forward

Utilizing this 3-dimensional on-lattice KMC to study ALD is an exciting and useful way to confirm the current theoretical understanding of the nuances of this process. As with any frontier, there is much work to be done. The following subsections outlay some important tasks that could further this research and the understanding of how KMC can accurately model ALD processes.

4.2.1. Al_2O_3 and Other Processes. It's clear from the Al_2O_3 simulations that, while the code can qualitatively simulate some of the relationships between growth parameters and the resultant sample, there are reactions missing from the reaction list and the incorporation of steric effects will be vital for simulations more in line with reality.

The work done in this thesis takes the torch from Shirazi and Weckman and carries it just a bit further. This does not mean that this code is incomplete. In fact, the code has served its intended purpose to establish a modeling KMC platform for ALD processes. One great advantage of building a stable KMC code is that, along the way, you get to experiment with turning on and off different reactions and thus evolve the code towards experimental conditions. This provides researchers an excellent opportunity to perform detailed studies of the reactions and compare their importance to accurately simulating the physical process of ALD.

However, as there are now three separates functional KMC models of this type, it is now clear that this method can be applied to numerous types of ALD. Metal-oxide materials with few species of atoms are excellent candidates for study via KMC, particularly of the one-to-one species ratio. Other forms of ALD such as the deposition of Al_2O_3 via TMA and ozone could also be a candidate for future KMC modeling [17,22].

More investigations can be done with ZnO and Al_2O_3 deposition by experimenting with different crystallographic orientations instead of exclusively using the (0001) direction. In order to perform this experiment, the energy barrier calculations must be rerun for all chemical reactions with the original slab replaced with one matching the desired crystallographic orientation.

4.2.2. KMC-TOOLS / Generalization. This method of modeling requires much preparation and a lot of the mundane heavy lifting was done with the help of Python scripts. An example of this is the KMC-ALD Simulation Starter. This graphical user interface allows the user to modify basic parameters of a template input script for the KMC code and produce multiple input scripts each with a different seed number for the KMC generator. Other Python scripts allow for rapid plotting of meaningful data, visualization of the simulation cell, and even partially automated creation of a lattice data file compatible with the KMC code.

More work needs to be done to generalize these tools so that they can be used reliably and interchangeably between the different types of ALD simulations. Ultimately, these scripts could be combined into a unified Python library so that future researchers could easily interact with their own KMC simulations. Once completed, these tools would make KMC modeling of ALD more accessible to researchers who might be interested in using this modeling technique. An example of a prototype GUI is depicted in Figure 34.

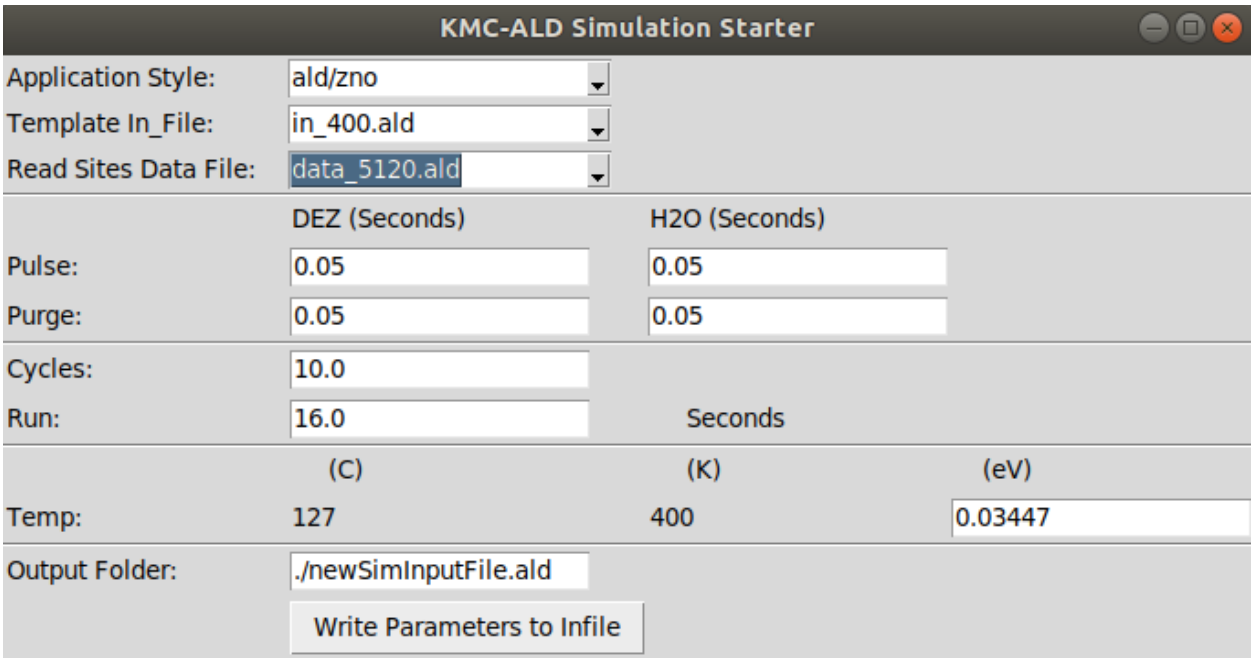

Figure 34. An image of the prototype KMC-ALD Simulation Starter tool capable of automatically modifying the parameters of a template input script to match the input desired by the user.

4.2.3. Resolving the Terminal Condition. The following is a proposed work-around to the terminal condition effect. It is possible, although cumbersome, to create a new initial surface by converting the last snapshot of data in the dump file. The simulation could be then restarted. By reversing the pulse sequence and starting with the opposite pulse as the previous simulation, the stagnated surface can again begin interacting as should occur in the physical deposition process. However, it is possible and likely that the same terminal condition will repeat making this not a practical option until this process can be automated with code.

4.2.5. FA-ALD. There is interest in Field Assisted Atomic Layer Deposition (FA-ALD). This is where an electric field is applied in the chamber during deposition [23]. The electric field may allow control of how the adsorbent molecules interact with the surface of the material. For example, water is a polar molecule and will orient itself along the direction of the electric

field. Hypothetically, this may alter the energy barriers for certain reactions. It is possible for GPAW to include a constant electric field in DFT calculation by passing the following argument to the GPAW calculator [15].

According to DFT calculations performed on a water molecule. Applying field of 1volt per Angstrom lengthened the OH bond from 0.971 Angstroms in no field to 0.973 Angstroms. Furthermore, the Gibbs Free Energy of the water molecule decreased from –14.66 eV to –15.06 eV. DFT calculations for the surface and the resultant surface with the adsorbed water molecule are still needed in order to conclude whether this field increased or decreased the overall energy barrier for this reaction.

In effect, a one line modification to every energy barrier calculation is all that would be required to calculate new energy barriers in the presence of en electric field. A simple update of the energy barriers in the reaction list would then make it possible to investigate the frontier of Field Assisted Atomic Layer Deposition with this KMC code.

4.2.6. ML Assisted Simulations. The results from the KMC simulations were compiled and used to train a machine learning model capable interpolating from simulated output data. The Machine Learning (ML) model was created using the Weka ML platform from the University of Waikato in New Zealand. Linear regression and multi-layer perceptrons can be employed with this software. Proposed here are two methods where ML could be handy in studying ALD.

4.2.6.A. Predicting Simulated ALD. Training a ML model presents two obvious advantages, the first being the ability to data mine and analyze the vast amounts of data that are produced by each simulation and multiplied by the number of simulations in each series. Manual analysis proves time-consuming and less fruitful than possible with the ML toolbox. The second

benefit of the ML is more application specific. As noted by Shirazi, computation time increases linearly with the number of sites in the simulation lattice, the computation time increases exponentially with temperature [10]. This means that high temperature runs, while theoretically possible with robust KMC models, become prohibitively expensive with regard to computation time. While we demonstrate the ability of this model to interpolate results, extrapolation of the data to higher temperatures would be a way to hybridize the KMC method with ML. The goal would be to have a ML model that can predict high temperature ALD results which could then be compared to experimental results.

4.2.6.B. ML for Faster DFT Calculations. Other research has been conducted to train ML models on data from DFT geometry optimization calculations [24]. Since DFT calculations can take inhuman amounts of time to perform it would be convenient if a ML model existed that could predict the DFT results in just a few seconds. Other researchers are beginning to employ this technique and it is only a matter of time before advances in this technique allow researchers to rapidly calculate energy barriers and would make the KMC method more accessible to researchers wishing to study ALD.

5. REFERENCES

[1] J. Acharya, "Effect of Al_2O_3 Seed-Layer on the Dielectric and Electrical Properties of Ultrathin MgO Films Fabricated Using In Situ Atomic Layer Deposition," *ACS Applied Materials Interfaces,* vol. 11, no. 33, pp. 30368-30375, 2019.

[2] R. Goul, R. Sakidja, and J. Wu, "Investigation of In Vacuo Atomic Layer Deposition of Ultrathin MgAl2O4 Using Scanning Tunneling Spectroscopy," *ACS Applied Electronic Materials,* vol. 2, no. 10, pp. 3121–3130, 2020.

[3] E. Guziewicz, "ALD grown Zinc Oxide with Controllable Electrical Properties," *Semiconductor Science,* 2012.

[4] P. Ramesh and M. Rincon, "Atomic Layer Deposition of Zinc Oxide," *Basic Solid State Physics*, vol. 257, no. 2, 2014.

[5] S. Shi, "Structural and Optical Properties of Amorphous Al_2O_3," *Condensed Matter Physics,* 2018.

[6] A. Philip, "Calculation of GPC of ALD," *Pramana,* vol. 82, pp. 563–569, 2014.

[7] S. Kimiesic, "Coarse Grained Molecules," *Chemical. Review,* vol. 116, no. 14, pp. 7898–7936, 2016.

[9] R. Dror, "Exploring Atomic Resolution Physiology on Femtosecond and Millisecond Timescale," Journal of General Physics, vol. 135, no. 6, 2010.

[10] M. Shirazi and S. Elliott, "Atomistic Kinetic Monte Carlo," *Journal of Computational Chemistry,* vol. 35, pp. 244-259, 2014.

[11] T. Weckman, "Kinetic Monte Carlo Study," *Journal of Chemistry,* vol. 122, no. 47, pp. 27044-27058, 2018.

[13] T. Weckman, "First Principles Alumina Deposition," *Physical. Chemistry,* vol. 17, pp. 17322-17334, 2015.

[14] Sandia National Laboratory, "SPPARKS Documentation," 2010. https://spparks.sandia.gov/doc/Manual.html

[16] A. Ciucivara, "Density functional studies of magnetic semiconductors and multiferroics," *University of Austin Texas,* 2007.

[17] J. Jur, G. Parsons and N. Gregory, ACS Applied Materials, vol. 3, no. 2, pp. 299-308, 2011.

[18] S. Hossein, "Anomalously High Alumina Atomic Layer Deposition," *Journal of Vacuum Science,* vol. 35, no. 1, 2017.

[19] M. Groner, "Low Temperature Al_2O_3 Atomic Layer Deposition," *Chemistry of Materials*, vol. 16, no. 4, pp. 639-645, 2004.

[20] C. Lie, "Mechanism for Al_2O_3 Atomic Layer Deposition," *Chemistry,* vol. 4, no. 10, pp. 2418-2435, 2018.

[22] D. Lancaster, "Atomic Layer Deposition of Zn Alloys," *Journal of Physical Chemistry,* vol. 121, no. 34, pp. 18643–186522017, 2017.

[23] W. Lu, "Preparation of ZnO Films with Variable Electric Field-Assisted Atomic Layer Deposition," *Applied Surface Science,* vol. 303, pp. 111-117, 2014

[24] R. Nagai, "Completing Density Functional Theory by Machine Learning," *Computational Mat*erials Science, vol. 6, no. 43, 2020.

[25] NIST, "Experimental Data for Water". *Computational Chemistry Comparison and Benchmark DataBase*, 2020. https://cccbdb.nist.gov/exp2x.asp?casno=7732185

[26] NIST, "Diethylzinc," *Chemistry Webbook,* 2018. https://webbook.nist.gov/cgi/cbook.cgi?Name=diethylzinc&Units=SI

[27] NIST, "Trimethyl-aluminum," *Chemistry Webbook,* 2018. https://webbook.nist.gov/cgi/cbook.cgi?ID=C75241&Mask=40

[28] M. Milovanovic, "How Flexible is the Water Molecule," *Physical Chemistry,* vol. 22, pp. 4138-4143, 2020.

[29] F. Alvi, "Coarse-Grained Kinetic Scheme-based Simulation," *Nanoparticle Research,* vol. 13, pp. 2451-2459, 2011.

[30] M. Mousa and C. Oldham, "Effect of Temperature and Gas Velocity," *Vacuum Science,* vol. 30, 2011.

[31] C. Dee, "Simulation for Deposition of ZnO via Kinetic Monte Carlo Method," *Materials Research Innovations,* pp.135-138, 2013.